The Astrophysical Journal, 935:177 (16pp), 2022 August 20 https://doi.org/10.3847/1538-4357/ac81c5

The ALPINE–ALMA [C II] Survey: The Infrared–Radio Correlation and Active Galactic Nucleus Fraction of Star-forming Galaxies at $z \sim 4.4$–5.9

Lu Shen[1,2], Brian C. Lemaux[3,4], Lori M. Lubin[4], Guilin Liu[1,2], Matthieu Béthermin[5], Médéric Boquien[6], Olga Cucciati[7], Olivier Le Fèvre[5], Margherita Talia[8], Daniela Vergani[7], Gianni Zamorani[9], Andreas L. Faisst[10], Michele Ginolfi[11], Carlotta Gruppioni[7], Gareth C. Jones[12,13,14,15], Sandro Bardelli[7], Nimish Hathi[16], Anton M. Koekemoer[16], Michael Romano[17,18,19], Daniel Schaerer[11], Elena Zucca[7], Wenjuan Fang[1,2], Ben Forrest[4], Roy Gal[20], Denise Hung[20], Ekta A. Shah[4], Priti Staab[4], Brittany Vanderhoof[21], and Eduardo Ibar[22]

[1] CAS Key Laboratory for Research in Galaxies and Cosmology, Department of Astronomy, University of Science and Technology of China, Hefei 230026, People's Republic of China; lushen@ustc.edu.cn
[2] School of Astronomy and Space Sciences, University of Science and Technology of China, Hefei 230026, People's Republic of China
[3] Gemini Observatory, NSF's NOIRLab, 670 N. A'ohoku Place, Hilo, Hawai'i, HI 96720, USA
[4] Department of Physics and Astronomy, University of California, Davis, One Shields Avenue, Davis, CA 95616, USA
[5] Aix-Marseille Université, CNRS, LAM (Laboratoire d'Astrophysique de Marseille) UMR 7326, F-13388 Marseille, France
[6] Centro de Astronomía (CITEVA), Universidad de Antofagasta, Avenida Angamos 601, Antofagasta, Chile
[7] INAF—Osservatorio di Astrofisica e Scienza dello Spazio di Bologna, via Gobetti 93/3, I-40129 Bologna, Italy
[8] University of Bologna—Department of Physics and Astronomy "Augusto Righi" (DIFA), Via Gobetti 93/2, I-40129, Bologna, Italy
[9] INAF—Osservatorio di Astrofisica e Scienza dello Spazio, Via Gobetti 93/3, I-40129, Bologna, Italy
[10] IPAC, M/C 314-6, California Institute of Technology, 1200 East California Boulevard, Pasadena, CA 91125, USA
[11] Observatoire de Genève, Universitè de Genève, 51 Ch. des Maillettes, 1290 Versoix, Switzerland
[12] Cavendish Laboratory, University of Cambridge, 19 J.J. Thomson Avenue, Cambridge, CB3 0HE, UK
[13] Kavli Institute for Cosmology, University of Cambridge, Madingley Road, Cambridge, CB3 0HA, UK
[14] Cavendish Laboratory/Kavli Institute for Cosmology, University of Cambridge, 19 J.J. Thomson Avenue, Cambridge, CB3 0HE, UK
[15] Department of Physics, University of Oxford, Denys Wilkinson Building, Keble Road, Oxford, OX1 3RH, UK
[16] Space Telescope Science Institute, 3700 San Martin Drive, Baltimore, MD 21218, USA
[17] National Centre for Nuclear Research, ul.Pasteura 7, 02-093 Warsaw, Poland
[18] Dipartimento di Fisica e Astronomia, Università di Padova, Vicolo dell'Osservatorio 3, I-35122, Padova, Italy
[19] INAF—Osservatorio Astronomico di Padova, Vicolo dell'Osservatorio 5, I-35122, Padova, Italy
[20] University of Hawai'i, Institute for Astronomy, 2680 Woodlawn Drive, Honolulu, HI 96822, USA
[21] School of Physics and Astronomy, Rochester Institute of Technology, Rochester, NY 14623, USA
[22] Instituto de Física y Astronomía, Universidad de Valparaíso, Avda. Gran Bretaña 1111, Valparaíso, Chile
Received 2021 November 25; revised 2022 July 12; accepted 2022 July 14; published 2022 August 24

Abstract

We present the radio properties of 66 spectroscopically confirmed normal star-forming galaxies (SFGs) at $4.4 < z < 5.9$ in the COSMOS field that were [C II]-detected in the Atacama Large Millimeter/submillimeter Array Large Program to INvestigate [C II] at Early times (ALPINE). We separate these galaxies ("C II-detected-all") into lower-redshift ("C II-detected-lz"; $\langle z \rangle = 4.5$) and higher-redshift ("C II-detected-hz"; $\langle z \rangle = 5.6$) subsamples, and stack multiwavelength imaging for each subsample from X-ray to radio bands. A radio signal is detected in the stacked 3 GHz images of the C II-detected-all and lz samples at $\gtrsim 3\sigma$. We find that the infrared–radio correlation of our sample, quantified by $q_{\rm TIR}$, is lower than the local relation for normal SFGs at a $\sim 3\sigma$ significance level, and is instead broadly consistent with that of bright submillimeter galaxies at $2 < z < 5$. Neither of these samples show evidence of dominant active galactic nucleus activity in their stacked spectral energy distributions (SEDs), UV spectra, or stacked X-ray images. Although we cannot rule out the possible effects of the assumed spectral index and applied infrared SED templates in causing these differences, at least partially, the lower obscured fraction of star formation than at lower redshift can alleviate the tension between our stacked $q_{\rm TIR}$s and those of local normal SFGs. It is possible that the dust buildup, which primarily governs the infrared emission, in addition to older stellar populations, has not had enough time to occur fully in these galaxies, whereas the radio emission can respond on a more rapid timescale. Therefore, we might expect a lower $q_{\rm TIR}$ to be a general property of high-redshift SFGs.

Unified Astronomy Thesaurus concepts: Star formation (1569); Submillimeter astronomy (1647); High-redshift galaxies (734); Galaxy evolution (734); Radio astronomy (594)

1. Introduction

A tight correlation between the total infrared (IR) and radio luminosity of star-forming galaxies (SFGs) has been known for decades, and was initially found to hold over three orders of magnitude for both IR and radio luminosity (e.g., de Jong et al. 1985; Helou et al. 1985; Condon 1992; Yun et al. 2001; Bell et al. 2003). Early observations have concluded that the IR–radio correlation (IRRC) does not appear to have evolved over the past 10–12 Gyr of cosmic history (e.g., Garrett 2002; Appleton et al. 2004; Ibar et al. 2008; Sajina et al. 2008; Garn et al. 2009; Murphy 2009; Jarvis et al. 2010; Sargent et al. 2010; Bourne et al. 2011; Mao et al. 2011; Smith et al. 2014). The IRRC is commonly quantified by the logarithmic ratio of the total IR (8–1000 μm) and 1.4 GHz luminosities ($q_{\rm TIR}$). Based on this tight IRRC, radio luminosity is well calibrated

and is used as a star formation rate (SFR) indicator (e.g., Condon 1992; Bell et al. 2003). Meanwhile, the excess of radio luminosity as compared to the IRRC has been used to identify active galactic nuclei (AGNs; e.g., Donley et al. 2005; Del Moro et al. 2013; Lemaux et al. 2014; Shen et al. 2017).

Star formation activity is known to be responsible for the existence of the IRRC, although the detailed physical mechanism and process remain unclear (e.g., Voelk 1989; Helou & Bicay 1993; Bell et al. 2003; Lacki & Thompson 2010). The IR originates from young massive stars that emit UV photons, which are absorbed by dust and reemitted in the IR region. The process is more complicated for the radio continuum emission, which originates from two components: (1) thermal emission from free–free interactions of ionized particles due to the H II regions surrounding recently formed high-mass stars; and (2) nonthermal synchrotron emission due to the supernovae of these stars after ∼10 Myr (e.g., Condon 1992). The radio continuum emission is expected to be modified at high redshift, due to the increasing typical interstellar medium (ISM) density and stronger magnetic fields, which in turn enhance the radio emission (Schleicher & Beck 2013). In addition, the smaller dust attenuation factor observed in high-redshift galaxies may affect the IRRC in terms of decreasing the expected IR emission (e.g., Carilli et al. 2008). Nevertheless, the contributions of AGNs to IR emission (e.g., Mor & Netzer 2012; Mullaney et al. 2012; Symeonidis et al. 2016; Lyu et al. 2017; Lyu & Rieke 2017) and to radio luminosity (e.g., Condon 1992; Del Moro et al. 2013) are known to affect the IRRC, as shown by the lower $q_{\rm TIR}$ value.

More recent studies have found a moderate, but statistically significant, evolution of the IRRC (Ivison et al. 2010; Casey et al. 2012; Magnelli et al. 2015; Calistro Rivera et al. 2017; Delhaize et al. 2017). In particular, Delhaize et al. (2017) have well quantified the evolution of $q_{\rm TIR}$ out to $z\sim3$ for SFGs using the deep 3 GHz data of Smolčić et al. (2017a) and Herschel data (Lutz et al. 2011; Oliver et al. 2012) in the Cosmic Evolution Survey (COSMOS) field. These results agree with the expected evolution of the IRRC, with an enhanced radio emission and/or a decreased IR emission at $z\sim3$. However, studies have found that the $q_{\rm TIR}$ depends on the radio luminosity (Molnár et al. 2021), the stellar mass (Gürkan et al. 2018; Delvecchio et al. 2021; Smith et al. 2021), and the observed radio frequency due to the different values of radio slope (An et al. 2021), with the dependence of these being stronger than that on redshift.

While attempts to quantify the IRRC for high-z SFGs ($z>3$) have been made, past studies have only investigated submillimeter galaxies (SMGs; Murphy 2009; Michałowski et al. 2010; Thomson et al. 2014; Smolčić et al. 2015; Miettinen et al. 2017; Algera et al. 2020). These studies have found that SMGs at high redshift ($z>2$) generally lie significantly below the canonical $q_{\rm TIR}$ ratio of local normal SFGs (Murphy 2009; Smolčić et al. 2015; Miettinen et al. 2017; Algera et al. 2020). However, SMGs provide only a biased view of the intensely star-forming population with SFR $>1000\ M_{\odot}\ {\rm yr}^{-1}$. Existing observations of radio and IR for normal SFGs, lying on the SFR–M_* relation for SFGs at these redshifts (e.g., Speagle et al. 2014; Tasca et al. 2015; Tomczak et al. 2016; Pearson et al. 2018; Khusanova et al. 2020), have not been conducted individually or statistically. The Atacama Large Millimeter/submillimeter Array (ALMA) Large Program to INvestigate C^+ at Early Times (ALPINE) survey provides measurements of the rest-frame far-IR (FIR) continuum emission for a representative sample of 118 normal SFGs at $4.4<z<5.9$. Using this data set, combined with the available deep radio observations for most of these galaxies, we here investigate the IRRC of normal high-z SFGs via a stacking analysis. In this paper, we present the ancillary data available for our sample and the sample selection in Section 2. In Section 3, we describe the stacking method and the spectral energy distribution (SED) fitting, which estimates the AGN contribution to the total IR luminosity ($f_{\rm AGN}$). Our results for the radio detection, the $q_{\rm TIR}$, and the fraction of the AGN component are presented in Section 4. We discuss a possible explanation for the lower $q_{\rm TIR}$ in Section 5. We conclude with a summary in Section 6. In this paper, we assume the Chabrier (2003) initial mass function (IMF) and a Λ cold dark matter cosmology, with $\Omega_\Lambda=0.7$, $\Omega_{\rm m}=0.3$, and $H_0=70\ {\rm km\ s^{-1}\ Mpc^{-1}}$.

2. Data and Sample Selection

2.1. ALPINE

ALPINE is a large ALMA program (Project ID: 2017.1.00428.L; PI: O. Le Fèvre; see also, e.g., Béthermin et al. 2020; Faisst et al. 2020b; Le Fèvre et al. 2020), which is aimed at measuring [C II] 158 μm and rest-frame FIR continuum emissions from a representative sample of 118 main-sequence galaxies at $4.4<z<5.9$. All galaxies are selected to be spectroscopically confirmed with rest-frame UV spectroscopy from the VIMOS Ultra Deep Survey (VUDS; Le Fèvre et al. 2015; Tasca et al. 2017) and the COSMOS 10K survey (Capak et al. 2004; Mallery et al. 2012; Hasinger et al. 2018) in the redshift range of $4.3<z_{\rm spec}<4.6$ and $5.1<z_{\rm spec}<5.9$. The gap in the redshift range is due to the presence of an atmospheric absorption feature. Galaxies were selected to have $\rm SFR_{SED}\geqslant10\ M_*\ yr^{-1}$ from COSMOS (105 galaxies; Scoville et al. 2007) and the Extended Chandra Deep Field South (ECDFS, 13 galaxies; Giacconi et al. 2002). Broad-line AGNs, identified by their rest-frame UV spectra, were not selected as ALPINE targets. One galaxy in the ALPINE sample was found to be detected at X-ray wavelengths, indicating AGN activity, though it is not a type-1 AGN (see Section 2.5 for more details). The construction and the physical properties of the sample are described in Faisst et al. (2020b) and Le Fèvre et al. (2020). The ALMA observations and the data reduction are fully described in Béthermin et al. (2020).

2.2. Radio Data

The ALPINE galaxies in the COSMOS field were covered by the Very Large Array (VLA) at 3 GHz, in the VLA-COSMOS 3 GHz Large Project (Smolčić et al. 2017a), and at 1.4 GHz, in several campaigns (Bertoldi et al. 2007; Schinnerer et al. 2007, 2010). The 3 GHz images were mapped with the VLA S band in the A and C configurations. The final 3 GHz images have a sensitivity of 2.3 μJy beam^{-1}, and the synthesized beam is 0.″75. A total of 10,830 sources were detected above 5σ, using the BLOBCAT software. The 1.4 GHz images were observed with the VLA L band in the A and C configurations, the synthesized beam being 1.″5 × 1.″4. The final 1.4 GHz images have a sensitivity of ∼8 μJy beam^{-1} in the central 30′ × 30′ and ∼12 μJy beam^{-1} over the full area, respectively (Karim et al. 2011). Using the AIPS task SAD, a total of 2865 sources were identified at $\geqslant5\sigma$ significance in the final VLA-COSMOS mosaic (Schinnerer et al. 2010). The ALPINE galaxies in the ECDFS field are only observed by the

VLA at 1.4 GHz. The final image has a best sensitivity of 6 μJy/beam. Using the AIPS task SAD and JMFIT, a total of 883 sources are identified at $\geqslant 4\sigma$ significance (Miller et al. 2013).

We cross-match the 3 GHz and 1.4 GHz sources to ALPINE galaxies using the 2″ search radius, separately. Only one ALPINE galaxy (DEIMOS_COSMOS_842313) is matched to a 3 GHz source (COSMOSVLA3 J100054.49+023436.2) in the 2″ search. It is known that DEIMOS_COSMOS_842313 has an extremely bright neighbor, identified as SC_2_DEIMOS_COSMOS_842313 in Béthermin et al. (2020), also known as J1000+0234 (Schinnerer et al. 2008) or AzTEC/C17 (Brisbin et al. 2017). This 3 GHz source is closer to SC_2_DEIMOS_COSMOS_842313, with a separation of 0.″12, as compared to 1.″17 to DEIMOS_COSMOS_842313, suggesting that the former is the match to the radio source. Thus, none of the ALPINE galaxies are individually detected in the 3 or 1.4 GHz images. In the absence of individual detections, we apply a stacking method, which is described in Section 3.1, to investigate the statistical radio properties of ALPINE galaxies.

2.3. FIR Data

The ALMA observations were conducted between 2018 May 7 (Cycle 5) and 2019 January 10 (Cycle 6), using antenna configurations C43-1 and C43-2. The integration times ranged from 15 to 45 minutes, with an average time of 22 minutes. The [C II] intensity maps and FIR continuum maps at rest-frame 158 μm were produced using the line and line-free channels, respectively (see the details in Béthermin et al. 2020). The resulting median sensitivity of the continuum maps is 41 μJy/beam, in the range of 16.8–72.1 μJy/beam. The average synthesized beam is $1.''13 \times 0.''85$.

2.4. Optical/IR Imaging

The existing imaging data for the ALPINE galaxies in the COSMOS and ECDFS fields are summarized in Faisst et al. (2020b). Briefly, these include B, V, g^+, r^+, i^+, and z^{++}, as well as 12 intermediate-band and two narrow-band filters from the Suprime-Cam on Subaru, the g, r, i, z, and y bands from the Hyper Suprime-Cam on Subaru, as well as the near-IR (NIR) bands Y, J, H, and Ks from VIRCAM on the VISTA telescope. All the ALPINE galaxies except one are observed in Advanced Camera for Surveys/Hubble Space Telescope F814W (Koekemoer et al. 2007; Scoville et al. 2007). In addition, the galaxies are covered by the four IRAC/Spitzer channels from 3.6 μm to 8.0 μm from the SPLASH survey[23] (Steinhardt et al. 2014; Laigle et al. 2016) and MIPS/Spitzer 24 μm from S-COSMOS (Sanders et al. 2007; Le Floc'h et al. 2009).

Nine ALPINE galaxies are covered by the NB2071 and NB2083 narrow-band imaging taken with the Multi-Object Infrared Camera and Spectrograph (Ichikawa et al. 2006; Suzuki et al. 2008) on the Subaru Telescope, as part of the Charting Cluster Construction with the VUDS (Le Fèvre et al. 2015) and ORELSE (Lubin et al. 2009) surveys (Lemaux et al. 2022; Shen et al. 2021). These observations are designed to target the [O II] emission in the massive protocluster PCl J1001+0220 at $z \sim 4.57$ and its surroundings in the COSMOS field (Lemaux et al. 2018). For more details of the data reduction, see Vanderhoof et al. (in preparation).

[23] http://splash.caltech.edu/

2.5. X-Ray Data

The Chandra-COSMOS Legacy Survey (Civano et al. 2016; Marchesi et al. 2016a) identified 4016 X-ray sources down to a flux limit of $f_X \sim 8.9 \times 10^{-16}$ erg s^{-1} cm^{-2} in the 0.5–10 keV band. The Chandra-COSMOS Legacy catalog was matched with the UltraVISTA catalog using the Likelihood Ratio technique (Sutherland & Saunders 1992), which provides a more statistically accurate result than a simple positional match (for more details, see Laigle et al. 2016). One ALPINE galaxy (DEIMOS_COSMOS_845652) was found to be an AGN detected with $L_{2-10\mathrm{keV}} = 10^{44.4}$ erg s^{-1}, using flux measured in the 0.5–2 keV band (corresponding to the rest frame of the 2–10 keV band at $z \sim 5$) and assuming $\Gamma = 1.4$, following Equation (4) in Marchesi et al. (2016b). Such luminosity places it in the AGN regime, with $L_{2-10\mathrm{keV}} = 10^{42}$ erg s^{-1} being the typical threshold for separating AGNs and SFGs (Marchesi et al. 2016c). Nevertheless, none of our results are affected by this galaxy, since all of our results are based on median stacking, which eliminates the possible effects of a single galaxy.

2.6. Spectra

The rest-frame UV spectroscopic data from which the ALPINE sample is selected are combined from various large surveys. Of the 105 ALPINE galaxies in the COSMOS field, 84 spectra are obtained from DEIMOS at the Keck Observatory in Hawaii (Capak et al. 2004; Mallery et al. 2012; Hasinger et al. 2018), and the remaining spectra are obtained from VIMOS at the VLT in Chile (Le Fèvre et al. 2005; Tasca et al. 2017). Their spectral resolutions are different, with R ~230 for VIMOS and R ~3200 for DEIMOS. See Faisst et al. (2020b) for more details on the spectra of ALPINE galaxies.

2.7. Sample Selection

We select the ALPINE galaxies in the COSMOS field that have [C II] detections at a signal-to-noise ratio (S/N) $\geqslant$3.5 (Béthermin et al. 2020). This [C II] detection criterion selects galaxies that are more likely to have usable radio and FIR fluxes, since the presence of [C II] both guarantees the redshift to be correct and increases the chance of appreciable FIR flux. Even so, this criterion potentially introduces selection bias. Both the median of the stellar mass and that of the SFR are increased by 0.1 dex relative to the full ALPINE sample when imposing the [C II] detection cut. In addition, this criterion might potentially bias galaxies having AGN activity. However, we applied various tests to our sample and did not find evidence of AGN activity, as discussed in Section 4.3. Of the total 118 ALPINE galaxies, the [C II] line is detected in 75 of them. We select galaxies only in the COSMOS field, due to the availability of the 3 GHz observation. Our final sample contains 66 ALPINE galaxies, including 43 galaxies at $z \sim 4.5$ and 23 galaxies $z \sim 5.6$. We name the galaxies in the full, lower-redshift, and higher-redshift samples as "C II-detected-all," "C II-detected-lz," and "C II-detected-hz," respectively. The median properties of each subsample are summarized in Table 1.

3. Methods

3.1. Image Stacking and Flux Measurements

Since none of the ALPINE galaxies are individually detected in the 3 and 1.4 GHz images, we carry out a stacking analysis. In order to systematically compare the radio luminosity with the IR

Table 1
Properties of the Three Subsamples

Subsample	Num. of (Galaxies)	$\langle z \rangle$	$\langle \log(M_*) \rangle$ ($\log(M_\odot)$)	$\langle \mathrm{SFR_{SED}} \rangle$ ($M_\odot$ yr^{-1})	$\langle \mathrm{SFR_{UV}} \rangle$ ($M_\odot$ yr^{-1}0	$\langle \mathrm{SFR_{IR}} \rangle$ ($M_\odot$ yr^{-1})	$\langle \mathrm{SFR_{tot}} \rangle$ ($M_\odot$ yr^{-1})
(1)	(2)	(3)	(4)	(5)	(6)	(7)	(8)
C II-detected-all	66	4.57	9.8	29.4	16.9	14.7	31.6
C II-detected-lz	43	4.54	9.8	31.9	16.6	24.6	41.2
C II-detected-hz	23	5.63	9.8	26.9	17.3	11.6	28.9

Note. Column (1): the name of the subsample. Column (2): the number of galaxies in each subsample. Column (3): the median of the spectroscopic redshift derived from [C II]. Columns (4)–(5): the median of the stellar mass and $\mathrm{SFR_{SED}}$ for each subsample derived from LE PHARE (see Faisst et al. 2020b). Column (6): the median of the $\mathrm{SFR_{UV}}$ using the absolute rest-frame FUV luminosity provided by the ancillary ALPINE catalog (Faisst et al. 2020b) and calculated by $\mathrm{SFR_{UV}} = k_{\mathrm{UV}} L_{\mathrm{FUV}}$, where $k_{\mathrm{UV}} = 1.47 \times 10^{-10}\, M_\odot\ \mathrm{yr}^{-1}\ L_\odot^{-1}$. Column (7): the median of the $\mathrm{SFR_{FIR}}$ using the L_{IR} measured from the median-stacked FIR image and following the method described in Section 4.2 (see also Béthermin et al. 2020). $\mathrm{SFR_{FIR}}$ is calculated by $\mathrm{SFR_{IR}} = k_{\mathrm{IR}} L_{\mathrm{IR}}$, where $k_{\mathrm{IR}} = 1.02 \times 10^{-10}\, M_\odot\ \mathrm{yr}^{-1}\ L_\odot^{-1}$. Column (8): the median of the $\mathrm{SFR_{tot}}$, by adding columns (6) and (7).

luminosity and perform SED fitting, we stack FIR continuum maps from ALMA and available optical/NIR/mid-IR (MIR) imaging. Two stacking methods that are commonly used are the mean or median. The former method is preferred for a population that exhibits an approximately Gaussian flux distribution, and requires the absence of close neighbors that contribute appreciable flux. On the other hand, median stacking is insensitive to the presence of outliers, and has the advantage that all the data can be used without qualifications from neighboring objects (e.g., Carilli et al. 2008; Karim et al. 2011; Man et al. 2016; Leslie et al. 2020), although it builds the S/N more slowly. As our data do not present ideal conditions for mean stacking, we adopt the median stacking method for all available bands.

We require accurate source positions in order to stack the images at the locations of the galaxies. Faisst et al. (2020b) measured the astrometric offset of the individual ALPINE galaxies between the COSMOS2015 catalog and the Hubble Space Telescope (HST) images that aligned to the Gaia reference frame. We adopt these Gaia-corrected coordinates as the locations of the galaxies for all images, except the 3 GHz images. A small systematic astrometric offset has been identified by a positional matching of the 3 GHz sources with the COSMOS2015 catalog, using a search radius of 0.″8 (Smolčić et al. 2017b). We use the optical position in COSMOS2015 after correcting for the systematic offset of the 3 GHz data using the best-fitting linear relations reported in Smolčić et al. (2017b).[24] Note that no astrometric offset has been found in the 1.4 GHz data. The relative and absolute astrometry of the 1.4 GHz image are 130 and <55 mas, respectively (Schinnerer et al. 2007). The relative astrometry is tested by comparing the positions of the sources extracted from each single pointing with those from the combined mosaic, and with those from the VLA FIRST survey catalog (Becker et al. 1995).

The stacking and detection are straightforward. For the galaxies in each subsample and each band, we create a $40'' \times 40''$ cutout of the image, centered on the applied coordinates of each galaxy. We then calculate the median-stacked image of $\mathrm{N_{objs}}$. To create stacked images free from projected bright sources, we remove sources detected above $>5\sigma$ significance, based on the 3 GHz catalog (Smolčić et al. 2017b), the 1.4 GHz catalog (Schinnerer et al. 2010), and the serendipitous detection catalog from Béthermin et al. (2020) for FIR. These sources are removed by fitting a 2D elliptical Gaussian within a $4'' \times 4''$ box, using the astropy fitting tools (Astropy Collaboration et al. 2013, 2018). These sources are found to be point sources in all radio and FIR images, by visual examination. This box size was then chosen based on the beam size of the radio/FIR images, so that it was slightly larger than these point sources. Except for one of 3 GHz sources, which was found to be 1.″17 away from an ALPINE galaxy (DEIMOS_COSMOS_842313), the separations between these point sources and our sample are larger than the beam sizes of the corresponding images, excluding the cases where the fluxes in the beam area of the ALPINE galaxies have been removed.

For the radio and FIR stacks, we adopt the CASA task imfit to measure the peak and total fluxes, by fitting one Gaussian component restricted to the central $3'' \times 3''$ box. The detection threshold is set to a peak three times above the local rms noise. For nondetections, we adopt 3σ as the upper limit, where σ is the rms of the stacked image obtained by the CASA task imstat, derived in the full $40'' \times 40''$ stacked image. For optical/NIR/MIR stacks, we adopt SExtractor (Bertin & Arnouts 1996) and measure the 3″ aperture flux at the center of each stacked image. The detection threshold is set to an aperture flux five times above the associated aperture flux error. For nondetections, we adopt 3σ as the upper limit, where σ is measured from the flux scatter of randomly distributed 3″ apertures. An additional flux correction is applied to IRAC images to obtain the total fluxes, following Ilbert et al. (2008). We show all of the stacked images for the C II-detected-all sample in Figure 5 in Appendix A.

To estimate the uncertainties on the stacked fluxes that represent the sample variance, we perform a bootstrap analysis by randomly drawing, with replacement, $\mathrm{N_{objs}}$ galaxy cutouts (from our initial list of galaxies) and creating a new median stack. We then measure the fluxes for each bootstrap stack using the same method as was used for the original stack. We repeat this process 100 times. When CASA imfit failed, such that no Gaussian component was successfully fitted, we adopted the 3″ aperture flux. It has been found that the fluxes obtained by 2D Gaussian fitting and aperture measurements are in excellent agreement overall (Béthermin et al. 2020). We adopt the 16th and 84th percentiles of the bootstrap fluxes as our errors on the peak and total fluxes, to represent the sample variance. Note that we do not apply a detection threshold for the bootstrap fluxes.

Using ALPINE data, Romano et al. (2021) found that a large fraction (∼40%) of [C II]-detected ALPINE galaxies are mergers. The majority of them have small projected distances

[24] $\mathrm{R.A.} = \mathrm{R.A._{L16}} + (-0.041\mathrm{R.A._{L16}} + 6.1)/3600$
$\mathrm{decl.} = \mathrm{decl._{L16}} + (0.058\mathrm{decl._{L16}} - 0.147)/3600.$

between the centers of the merger components ($r_p \lesssim 10$ kpc), as found by inspecting their [C II] intensity maps. Thus, we expect the majority of the components in these mergers to be covered by the 3″ box (corresponding to 19 kpc at $z = 5$) for radio/FIR images or the 3″ aperture for optical/NIR images. The widespread presence of such merging activity may introduce smearing and offsets in the radio images, which might be one of the reasons that we observe offsets in our radio-stacked images (see Section 4.1).

3.2. Estimating the AGN Contribution and SFR from SED Fitting

We employed the SED fitting Code Investigating GALaxy Emission (CIGALE; Boquien et al. 2019) in order to constrain the AGN contribution to the IR luminosity of our stacked samples, in a self-consistent framework that considers the energy balance between the UV/optical and the IR. We set the templates and parameters in CIGALE to be consistent with the previous SED fitting for ALPINE galaxies that was done with LE PHARE (Arnouts et al. 1999; Ilbert et al. 2006), as described in Faisst et al. (2020b). In detail, we adopted a delayed exponential star formation history (SFH; sfhdelayed), allowing the range of τ and age to be similar to those used in Faisst et al. (2020b). We assumed a Chabrier (2003) IMF and the stellar population synthesis models presented by Bruzual & Charlot (2003), with solar ($Z_\odot$) and 0.2 $Z_\odot$ metallicity. The dust attenuation follows the Calzetti et al. (2000) extinction law, allowing the color excess $E_s(B-V)$ to vary from 0 to 0.5. Note that the absorption UV bump feature produced by dust at 2175 Å is set to zero, because the stacked SEDs do not have enough spectral resolution to meaningfully constrain it. For the dust emission module, we adopted the dust templates of Draine et al. (2014), to remain consistent with the best-fit IR SED template found for ALPINE analogs in the COSMOS field, which was used to derive the IR luminosity from the rest-frame 158 μm continuum fluxes (Béthermin et al. 2020). This best-fit IR SED template has a mean intensity of the radiation field $\langle U \rangle = 50$, with fixed values of the maximal radiation field ($U_{\rm max} = 10^6$), the fraction illuminated from $U_{\rm min}$ to $U_{\rm max}$ ($\gamma = 0.02$), the power-law index ($\alpha = 2$), and the polycyclic aromatic hydrocarbons (PAH = 2.5%; Magdis et al. 2012; Béthermin et al. 2015, 2017). Following this best-fit IR SED template, we set the parameters in the dust model, only allowing the the minimal radiation field $U_{\rm min}$ to vary from 30 to 40, corresponding to $\langle U \rangle = 37$–50.

For the AGN module, we adopt the latest SKIRTOR template that is implemented in CIGALE (Yang et al. 2020). We retain the default parameters in the AGN module, other than setting the viewing angle i to 30° and 70° for type-1 and type-2 AGNs, respectively, and the full range of AGN fraction ($f_{\rm AGN}$) from 0 to 0.9, a fraction that denotes the contribution from the AGN to the total IR luminosity (Ciesla et al. 2015). We note that only two viewing angles are selected, in order to obtain the most informative parameters. Ramos Padilla et al. (2022) have tested the effect of the viewing angles in AGN classification, and found that limiting the viewing angles representing these two types of AGNs (30°/70°) does not affect the estimated physical parameters (i.e., $f_{\rm AGN}$) as compared to using the full range of viewing angles.

For radio synchrotron emission, either from star formation or AGNs, we allow the $q_{\rm TIR}$ to vary in the range of 1.5 to 3.0, to cover the $q_{\rm TIR}$ of local normal SFGs (Bell et al. 2003) and those expected for SFGs and/or AGNs at $z \sim 5$ (Delhaize et al. 2017). We adopt a single spectral slope of power-law synchrotron emission $\alpha_{\rm radio} = 0.7$, since we do not have detections in enough radio bands to constrain the radio spectral slope (see the discussion of the selection of α in 4.1).

Finally, we adopt the "pdf analysis" method in CIGALE to compute the likelihood (χ^2) for all the possible combinations of parameters, and generate the marginalized probability distribution function for each parameter and each galaxy stack. More details of the parameter settings are shown in Table 2. In addition, we adopt a mock analysis in CIGALE to derive the uncertainty of the estimated parameters, based on the photometric errors. The mocks are built based on the best fit for each object, and are modified by sampling from a Gaussian distribution with the same standard deviation as the uncertainty on the observation. For further discussion of this method, see the Appendix of Shen et al. (2020). We generate 100 mocks for each stacked SED and adopt the 16th/84th percentiles as the uncertainty on each parameter.

We run CIGALE on the photometry measured from the stacked ground-based observations in u, B, V, r^+, i^+, z^{++}, Y, $Y_{\rm HSC}$, $J_{\rm HSC}$, $H_{\rm HSC}$, $H_{\rm HSC}$, Ks, the intermediate bands IA427, IA464, IA484, IA505, IA527, IA574, IA624, IA679, IA709, IA738, IA767, and IA827, as well as from the space-based observations in F814W/HST, all four IRAC/Spitzer channels, and MIPS/Spitzer at 24 μm. The best-fitting models of the three stacked SEDs are shown in Figure 3. The reduced χ^2 of the best-fitting SEDs are 1.5, 0.71, and 0.70 for the C II-detected-all, C II-detected-lz, and C II-detected-hz stacks, respectively. We note that the redshift of C II-detected-all is set to its median spectroscopic redshift $z = 4.57$, but the stacked SED includes galaxies from $z = 5.5$, which might

Table 2
Parameter Ranges Used in the SED Fitting with CIGALE

Parameter	Values
SFH sfhdelayed	
τ [Myr]	100, 500, 1000, 3000
Age [Myr]	50–1100
Simple Stellar Populations (Bruzual & Charlot 2003)	
IMF	Chabrier (2003)
Metallicity ($Z_\odot$)	1, 0.02
Dust Attenuation (Calzetti et al. 2000)	
$E(B-V)_l$	0.0–1.1
$E(B-V)_{factor}$	0.44
Slope of the power law	−0.5, -0.25, 0
Dust Emission (Draine et al. 2014)	
Mass fraction of PAH	2.5%
Minimum radiation field	30, 35, 40
Power slope $dU/dM \propto U^{-\alpha}$	2.0
Dust fraction in photodissociation regions	0.02
AGN Emission	
θ	30, 70
$f_{\rm AGN}$	0–0.9
Radio Emission	
$q_{\rm IR}$	1.5, 1.75, 2.0, 2.25, 2.5, 3.0
α	0.7

be the reason for the larger reduced χ^2. We note that, with our current photometry data set, we are not able to constrain the AGN and dust emission at the same time. Therefore, we only allow a small variation on the dust module, to remain consistent with the best-fit IR SED template from Béthermin et al. (2020), so that the CIGALE fitting was performed mainly to estimate two parameters ($f_{\rm AGN}$ and viewing angle) associated with the AGN module. The former is defined as the AGN contribution to IR luminosity ($L_{\rm AGN} = f_{\rm AGN} \times L_{\rm IR}$; Ciesla et al. 2015). The later separates the typical AGN templates for type-1 and type-2 AGNs. As a sanity check, we compare the stellar mass and SFR from the stacked SEDs using CIGALE and the median of them from the ancillary ALPINE catalog derived from LE PHARE. Though we observe some differences in the recovered parameters from the stacked CIGALE fitting and the median parameters of the LE PHARE fitting for various stacked samples, none of the differences are statistically significant.

4. Results

4.1. Radio Detection and Luminosity

In Figure 1, we show the $10'' \times 10''$ median-stacked 3 GHz images of C II-detected-all, C II-detected-lz, and C II-detected-hz, from left to right, respectively, and the corresponding histograms of the bootstrap total fluxes in the bottom panels. We successfully detect a signal in the stacked 3 GHz images of C II-detected-all and C II-detected-lz, with their peak fluxes at 3.2σ and 3.9σ, respectively, where σ is the associated error on the peak fluxes. No significant detection ($>3\sigma$) is obtained in the stacked 3 GHz image of C II-detected-hz, which is most likely due to the smaller number of galaxies in the C II-detected-hz sample. To test this, we randomly select 23 galaxies from the C II-detected-all sample, the same number of galaxies in the C II-detected-hz sample, without replacement, and apply the same median stacking and flux measurement. We do not recover any significant detection in the majority (73%) of the iterations. In addition, none of these subsamples are significantly detected in their stacked 1.4 GHz image. The fluxes and uncertainties from the bootstraps are shown in Table 3. We also test using mean stacking, which directly increases the S/N of an image as $\sqrt{n}$, where n is the number of galaxies. We obtain higher significant detections for C II-detected-all and C II-detected-lz, with their peak fluxes at 4.7σ and 6σ, respectively. We note these increased S/Ns only for statistical argument, as they are likely to be contaminated by neighbors at much higher significance levels. In addition, we recover stacked 3 GHz fluxes that are statistically identical using the position of [C II] emission (see Table C.1 in Béthermin et al. 2020), done without the coordinate correction described in Section 3.1. It should be noted that we do not detect a signal in the stacked 3 GHz image when including all the ALPINE galaxies, which is most likely due to the fainter sources diluting the signal in the stacks.

Though we use the peak flux for detection significance, the total fluxes are adopted because we see an elongated shape in our stacked image. The elongated shape might be due to various astrophysical and astrometric effects that cause an effective blurring of the stacked image. The astrophysical effects might be the dominant causes, due to the presence of mergers in our sample, the physical extent of the SFGs, and a possible offset between optical and radio sources. In fact, it has previously been found that the physical extent of SFGs at 3 GHz is 1–2 kpc out to $z \sim 2.25$ (Jiménez-Andrade et al. 2019), which corresponds to $0\farcs15$–$0\farcs3$ at $z = 4.6$. In addition, it could also be affected by subpixel variations between images. For example, a small ($0\farcs1$) astrometric offset persists between the optical catalog and the true 3 GHz source position after correcting for the systemic offset (Smolčić et al. 2017b). Therefore, we use the total flux densities as our final radio fluxes.

The measured 3 GHz flux densities ($S_{\rm 3GHz,total}$) are converted to rest-frame 1.4 GHz luminosities via

$$L_{\rm 1.4GHz} = \frac{4\pi D_L^2}{(1+z)^{1+\alpha}} \left(\frac{1.4{\rm GHz}}{3{\rm GHz}}\right)^{\alpha} S_{\rm 3GHz}, \quad (1)$$

where D_L is the luminosity distance to the galaxy and α is the spectral index. Because all three subsamples were not detected at 1.4 GHz, we calculate the lower limit on the spectral index, as listed in Table 3. Smolčić et al. (2017a) cross-matched the 3 GHz catalog with the 1.4 GHz catalog in COSMOS, with a maximum separation of $1\farcs3$, and obtained a spectral index of, on average, $\alpha = -0.73 \pm 0.35$. Smolčić et al. (2017c) showed that the spectral index tends to be steeper with increasing redshift. However, such a trend might not be robust at high redshift, due to the small sample of galaxies at $z \geqslant 3$, the flux limitations on these observations, and, at higher rest-frame frequency with increasing redshift, the spectral index becoming flatter due to free–free emission dominating the radio emission. Delhaize et al. (2017) further selected SFGs in the combined 3 GHz and 1.4 GHz catalogs, and quantified the median spectral index of the SFGs to be -0.7 at $z < 2$ and -0.8 at $z > 2$. These two spectral index values are the typical values used for radio sources. This α value is consistent with that found in the sub-mJy radio population (Ibar et al. 2009), submillimeter galaxies at $z \sim 2$ (Ibar et al. 2010), and the lower limits of α from the ALPINE subsamples. Therefore, we adopt a simple $\alpha = -0.7$ in the calculation of the rest-frame 1.4 GHz luminosity. We examine the possible effect on $q_{\rm TIR}$ using a steeper and flatter spectral index ($\alpha = -0.8$, $\alpha = -0.6$) in Section 5.

Radio luminosity can be used as an SFR indicator for SFGs. We estimated the radio-derived SFR ($\rm SFR_{radio}$) by using the SFR formula for 1.4 GHz from Bell et al. (2003) and converting the Salpeter IMF to the Chabrier IMF by multiplying by a factor of 0.6. The $\rm SFR_{radio}$ are 147^{+136}_{-78}, 193^{+271}_{-142}, and $<200\ M_\odot\ {\rm yr}^{-1}$ for C II-detected-all, lz, and hz, respectively. The uncertainties are derived from the average of the 16th/84th percentiles of bootstrap radio fluxes. These values are considerably larger than the average total SFR measured by combining ALPINE continuum stacking and ancillary UV data, as shown in Table 1. Specifically, using the stacked FIR fluxes and the median far-UV (FUV) luminosity, $\rm L_{FUV}$, provided by the ancillary ALPINE catalog (Faisst et al. 2020b), and following Equation (9) in Béthermin et al. (2020), we calculate full SFRs ($\rm SFR_{tot}$) of 32 ± 14, 41 ± 18, and $29 \pm 21\ M_\odot\ {\rm yr}^{-1}$ for C II-detected-all, lz, and hz, respectively. The uncertainties are the average of the 16th/84th percentiles of the bootstrap FIR fluxes and the 16th/84th percentiles of $L_{\rm FUV}$. Although the differences between the radio- and UV+IR-derived SFRs are not statistically significant, mostly due to the extremely large errors of the former estimate, such differences may suggest that either an appreciable AGN component exists, which contributes to the radio luminosity, or that the $\rm SFR_{radio}$ formula, which is calibrated based on the local IRRC, might not be appropriate for these galaxies, or some combination thereof.

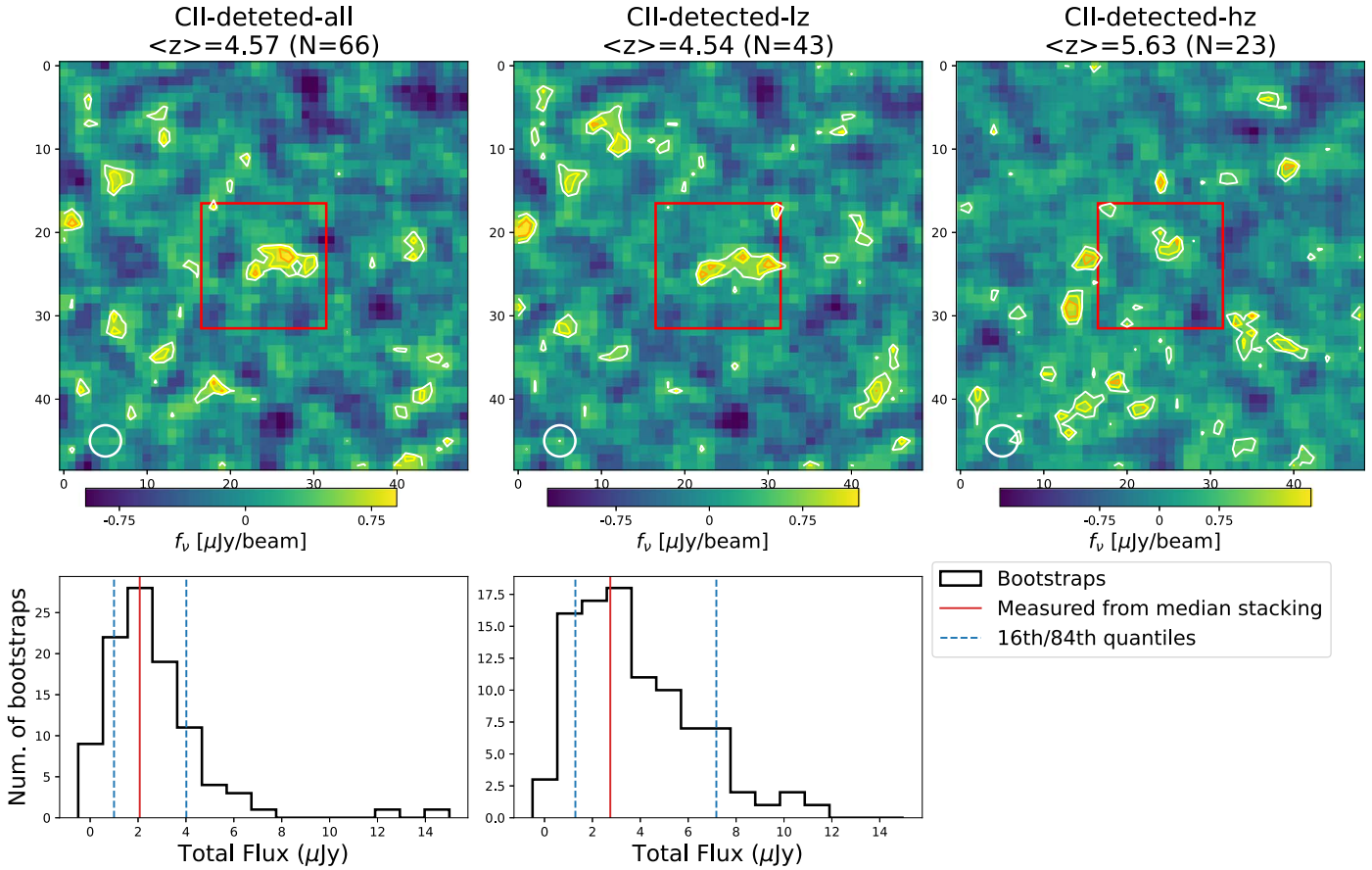

Figure 1. Top: the $10'' \times 10''$ median-stacked 3 GHz images of the C II-detected-all, C II-detected-lz, and C II-detected-hz samples (see the text for the meanings of these samples), from left to right. In each panel, the black contours show 1.5, 2, and 2.5 × rms obtained by the CASA task IMSTAT in the full stack image. The central $3'' \times 3''$ box used for detection is marked in red, and the $0''.75$ beam is shown in the bottom left corner. Bottom: the corresponding histograms of the bootstrap total fluxes obtained from 100 bootstrap stacks for the C II-detected-all and C II-detected-lz samples. In each panel, the measured total flux and 16th/84th percentiles of the bootstrap fluxes are shown as the solid red and dotted green lines, respectively. The histogram of C II-detected-hz is not shown, since no detection is obtained in the original stacking and in the most of the bootstrap stacking realizations.

Table 3
Radio Flux Densities at 3 and 1.4 GHz

Subsample	$S_{3\mathrm{GHz,peak}}$ (μJy/beam)	$S_{3\mathrm{GHz,total}}$ (μJy)	$\mathrm{rms}_{3\mathrm{GHz}}$ (μJy/beam)	$\mathrm{rms}_{1.4\mathrm{GHz}}$ (μJy/beam)	$\alpha_{1.4-3\ \mathrm{GHz}}$	$L_{1.4\mathrm{GHz}}$ (10^{24} W Hz^{-1})
(1)	(2)	(3)	(4)	(5)	(6)	(7)
C II-detected-all	$1.08^{+0.56}_{-0.21}$	$2.07^{+1.92}_{-1.10}$	0.36	1.94	$\geqslant -1.35$	$0.44^{+0.41}_{-0.24}$
C II-detected-lz	$1.21^{+0.68}_{-0.20}$	$2.75^{+3.87}_{-2.02}$	0.44	2.38	$\geqslant -1.25$	$0.58^{+0.82}_{-0.43}$
C II-detected-hz	⋯	⋯	0.61	3.02	$\geqslant -2.11$	<0.60

Note. Column (1): the name of the subsample. Columns (2) and (3): the peak and total fluxes measured in the 3 GHz stack images; the associated errors are the 16th and 84th percentiles of the bootstrap fluxes. Columns (4) and (5): the rms of the 3 and 1.4 GHz stack images. Column (6): 3σ lower limit of the spectral index. Column (7): rest-frame 1.4 GHz luminosity for C II-detected-all/lz and 3σ upper limit for C II-detected-hz.

Therefore, we further investigate the IRRC of our sample as compared to other studies in the literature, in Section 4.2, and possible AGN contamination, in Section 4.3.

4.2. The IRRC

The IRRC can be quantified by the parameter q_{TIR}, defined as the logarithmic ratio of the total IR (8–1000 μm) and 1.4 GHz luminosities:

$$q_{\mathrm{TIR}} = log\left(\frac{L_{\mathrm{TIR}}/\mathrm{W}}{3.75 \times 10^{12}\mathrm{Hz}}\right) - log\left(\frac{L_{1.4\mathrm{GHz}}}{\mathrm{W\ Hz^{-1}}}\right), \quad (2)$$

where L_{TIR} is the rest-frame total IR (8–1000 μm) luminosity and $L_{1.4\mathrm{GHz}}$ is the rest-frame radio luminosity at 1.4 GHz (Condon 1992; Bell et al. 2003). We use the same method as Béthermin et al. (2020) to convert the rest-frame 158 μm stack flux to L_{TIR}. Béthermin et al. (2020) identified the best-fit IR SED template by fitting to a mean-stacked continuum FIR SED for ALPINE galaxy analogs in terms of redshift, stellar mass, and SFR in the COSMOS field.

The q_{TIR} are $1.52^{+0.35}_{-0.27}$ and $1.63^{+0.41}_{-0.34}$ for C II-detected-all and lz, respectively, with a lower limit of 1.29 for C II-detected-hz. The lower/upper uncertainties of the q_{TIR} are the difference between the 16th/84th percentiles and the median of the q_{TIR} distribution,

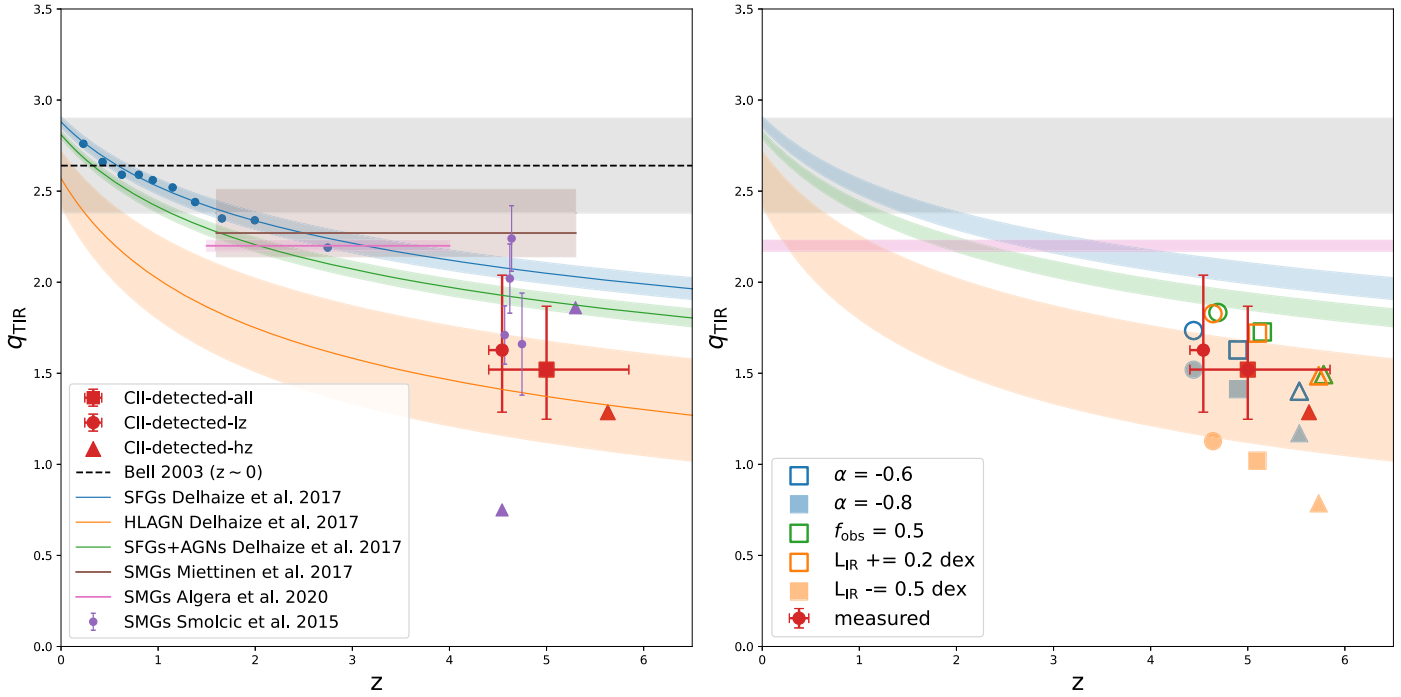

Figure 2. Left: the stacked $q_{\rm TIR}$ vs. median redshift for the three ALPINE subsamples, as compared to the literature. The measured $q_{\rm TIR}$ of C II-detected-all/lz are shown as the red dot and square, with error bars. The 3σ lower limit of C II-detected-hz is shown as the triangle. The $q_{\rm TIR}$ errors include the spread of the IR and radio fluxes obtained from bootstrapping. The redshift error bars represent the redshift range in each subsample. The blue dots are the median $q_{\rm TIR}$ for SFGs, binned by the redshift adopted from Delhaize et al. (2017). The blue solid line is the power-law fit and error, shown as the shaded region. The green and orange lines and shaded regions are the best power-law fits and associated errors for all galaxies (labeled as "SFGs+AGNs") and for HLAGNs only (Delhaize et al. 2017). The dotted black line and shaded region are the local value of Bell et al. (2003; $q_{\rm TIR}$ ($z \sim 0$) $= 2.64 \pm 0.02$) and the associated spread of 0.26, respectively. The brown and pink lines show the median $q_{\rm TIR}$ measured for SMGs at $z = 1.6$–5.3 (Miettinen et al. 2017) and at $z = 1.5$–4 (Algera et al. 2020), respectively. The purple markers are adopted from Smolčić et al. (2015), with the triangles representing the lower limits. Right: the fiducial $q_{\rm TIR}$ for the three ALPINE subsamples. The measured/lower limit $q_{\rm TIR}$ are shown as the solid red markers with error bars. The fiducial $q_{\rm TIR}$ are shown as: blue open markers for using $\alpha = -0.6$; blue shaded markers for using $\alpha = -0.8$; orange open markers for increasing the $L_{\rm IR}$ by 0.2 dex, due to different IR SED templates; orange shaded markers for decreasing the $L_{\rm IR}$ by 0.5 dex, due to different IR SED templates; and green open markers for applying a correction on the obscured fraction of star formation (see Section 5). The points are offset in redshift for clarity. The shaded regions are the same as those shown in the right panel, for direct comparison.

as calculated from the IR and radio bootstrapping fluxes, which represents the sample variance. Note that the systematic uncertainty of assuming a single FIR SED is not accounted for here (this is done in Section 5). Figure 2 shows the stacked $q_{\rm TIR}$ and associated uncertainties versus the median redshift of the three ALPINE subsamples. For clarity, the redshift of C II-detected-all is offset from its median value ($z = 4.57$). The error bar on the x-axis represents the redshift range of each subsample. Note that we do not consider AGNs in the calculation of $q_{\rm TIR}$. Although the data are not sufficient to confirm whether AGNs contribute to the radio band, either through spectral index or SFR estimates, we do not find evidence of dominant AGN activity in the optical-to-FIR SED, X-ray, and UV spectra. See the further discussion related to AGNs in Section 4.3.1.

We compare our results for $q_{\rm TIR}$ to several other studies in the literature. First, a $q_{\rm TIR} = 2.64 \pm 0.02$ with a scatter of 0.26 dex was measured by Bell et al. (2003) in 162 local normal SFGs . Our measured $q_{\rm TIR}$ are clearly offset from the $q_{\rm TIR}$ of local SFGs, even considering their large error bars. More specifically, the $q_{\rm TIR}$ of the C II-detected-all and C II-detected-lz subsamples are offset from the local $q_{\rm TIR}$ value by 3.2σ and 2.5σ, where σ includes the uncertainties on the $q_{\rm TIR}$ of the ALPINE subsamples and that of the local SFGs. More recently, Delhaize et al. (2017) quantified $q_{\rm TIR}$ out to $z \sim 3$, using the same 3 GHz image as this paper and Herschel data (Lutz et al. 2011; Oliver et al. 2012) in the COSMOS field. They employed a doubly censored survival analysis to include both lower and upper limits, and quantified the evolution of $q_{\rm TIR}$ for SFGs, all galaxies (including SFGs and AGNs), and only moderate-to-high radiative luminosity AGN (HLAGN) samples. The $q_{\rm TIR}$ of the ALPINE subsamples are consistent with this trend, though our values tend toward the lower end of the $q_{\rm TIR}$ range of models, where some AGN contribution exists.

It has also been found that the $q_{\rm TIR}$ of SMGs at high redshift ($z > 1.5$) are in general lower than the local values for normal SFGs (Murphy 2009; Michałowski et al. 2010; Thomson et al. 2014; Smolčić et al. 2015; Miettinen et al. 2017; Algera et al. 2020). Miettinen et al. (2017) studied the physical properties of 16 SMGs in the redshift range of $z = 1.6$–5.3 in the COSMOS field. They found a median $q_{\rm TIR}$ of $2.27^{+0.27}_{-0.13}$, shown as the brown line, with the 16th–84th quantiles as the shaded region, using a radio luminosity derived from 325 MHz (corresponding to the rest-frame 1.4 GHz at $z = 3.3$) and an IR luminosity derived from the SED fitting by the MAGPHYS code. Recently, Algera et al. (2020) measured the $q_{\rm TIR}$ of 273 SMGs that have 1.4 GHz detections, and found a median $q_{\rm TIR} = 2.20 \pm 0.03$ independent of redshift, shown as the pink line and shaded region. In addition, Smolčić et al. (2015) measured the $q_{\rm TIR}$ of six spectroscopically confirmed SMGs at $z > 4$ in the COSMOS field. Using survival analysis, they found a mean and standard derivative $q_{\rm TIR} = 1.95 \pm 0.2$. The $q_{\rm TIR}$ of Smolčić et al. (2015) are shown as purple dots with error bars, and their upper limits are shown as triangles. We see that our stacked $q_{\rm TIR}$ are consistent with the values from Smolčić et al. (2015) and broadly in line with the trend of Miettinen et al. (2017) and Algera et al. (2020), within the errors. However, we point out that the physical properties of these SMGs, such as stellar mass and SFR, are extremely different from the

galaxies in ALPINE. The average stellar mass and the range of the SFR of the SMGs in Smolčić et al. (2015) are $1.4 \times 10^{11} M_{\odot}$ and 600–2000 $M_{\odot}$ yr^{-1}, respectively, both well in excess of those values of the ALPINE galaxies studied here. That our stacked $q_{\rm TIR}$ is lower than the $q_{\rm TIR}$ values for normal SFGs potentially indicates an AGN contribution and/or that lower $q_{\rm TIR}$ values are a general property of high-redshift ($z > 4$) SFGs.

4.3. Possible AGN Contribution

While powerful broad-line AGNs were selected against when constructing the ALPINE sample, the prevalence of AGNs was previously unknown. To address the possible AGN contribution to the $q_{\rm TIR}$, we apply three approaches: SED fitting using stacked multiwavelength photometry, stacking X-ray data, and rest-frame UV spectra.

4.3.1. AGN Fraction

First, we quantify the fraction of AGN contribution to IR luminosity using CIGALE for the stacked SEDs of the three ALPINE subsamples. The best-fitting $f_{\rm AGN}$ are $0.00^{+0.18}$, $0.15^{+0.30}_{-0.15}$, and $0.18^{+0.52}_{-0.18}$ for the C II-detected-all/lz/hz subsamples, where the uncertainties of $f_{\rm AGN}$ are the 16th/84th percentiles of 100 mocks, regardless of AGN type. The stacked SEDs for C II-detected-lz and C II-detected-hz are best fitted to type-2 AGNs, with a viewing angle of 70°, and type-1 AGNs, with a viewing angle of 30°, respectively. The corresponding bolometric $L_{\rm AGN}$ from the best-fitting models of C II-detected-lz and hz subsamples are both $10^{44.2}$ erg/s, though their $f_{\rm AGN}$ are statistically consistent with no AGN activity. The upper limits of $L_{\rm AGN}$ from the type-1/2 mocks are $10^{44.7}/10^{45.0}$ erg/s, $10^{44.7}/10^{45.5}$ erg/s, and $10^{44.7}/10^{45.6}$ erg/s for the C II-detected-all, lz, and hz subsamples, respectively.

In the bottom right panel of Figure 3, we show histograms of the $f_{\rm AGN}$ mocks separated into type-1 and type-2 AGNs, based on their fitted viewing angles, as well as the best-fitting $f_{\rm AGN}$ for the three subsamples. The stacked SEDs of all three subsamples are best fitted to little to no AGN activity, and their mocks almost exclusively populate the lower-$f_{\rm AGN}$ ($f_{\rm AGN} \leqslant 0.2$) regions. The statistical mode of all $f_{\rm AGN}$ is zero for the mocks of all three subsamples, suggesting that these subsamples on average have little to no AGN activity. In addition, the C II-detected-lz/hz subsamples are best fitted to slightly higher $f_{\rm AGN}$, but consistent with that of the C II-detected-all sample within 1σ. Although we note that the mocks of C II-detected-lz/hz span the full $f_{\rm AGN}$ range, which indicates that larger $f_{\rm AGN}$ values are possible, though still unlikely.

We note a caveat that the estimated $f_{\rm AGN}$ might be limited and potentially biased low, due to the lack of NIR/MIR constraint and the wavelength range (i.e., total IR) chosen by CIGALE to estimate the AGN fraction, where the contribution from the galaxy might dilute any AGN contribution. Nevertheless, we find that, with the current photometry data, CIGALE can effectively recover the full $f_{\rm AGN}$ range for type-1 AGNs and high $f_{\rm AGN}$ values for type-2 AGNs, while underestimating the values of low-to-moderate type-2 AGNs by a factor of 2 (for more discussion, see Appendix B). Furthermore, the best-fitting $f_{\rm AGN}$ do not change significantly if the X-ray-detected galaxies are excised from the C II-detected-all and hz subsamples.

4.3.2. Test on X-Ray Observations

Second, we stack the X-ray observations, which might provide a more direct signal if AGNs exist, especially for type-1 AGNs, where the X-ray emission is not obscured by a dusty AGN torus (Padovani et al. 2017). We use the publicly available CSTACK4[25] tool to stack Chandra soft-band ([0.5–2] keV) and hard-band ([2–8] keV) X-ray images of the galaxies in each subsample (Miyaji & Griffiths 2008). We exclude the X-ray-detected galaxy in the C II-detected-all and hz subsamples. In order to diagnose the X-ray luminosity of the nondetections by stacking, none of subsamples show a $>3\sigma$ detection in either band. Our stacked X-ray observations for C II-detected-all are down to uncertainties of $f_X = 2.1 \times 10^{-17}$ erg s^{-1} cm^{-2} in [0.5–2] keV, assuming a power-law X-ray spectrum with a slope of 1.4 and a galactic N_H value of 2.6×10^{20}cm^{-2}. The corresponding 3σ upper limit of the rest-frame X-ray luminosity is $L_{2-10\rm keV} = 10^{43.1}$ erg s^{-1}. These values are comparable to a moderate Seyfert, where $L_{2-10\rm keV} = 10^{42}$ erg s^{-1} and 10^{44} erg s^{-1} are the typical thresholds for separating between SFGs/AGNs and Seyferts/quasars, respectively (Marchesi et al. 2016c). Adopting the bolometric correction of X-ray luminosity for radio-quiet AGNs from Runnoe et al. (2012), we obtain a 3σ upper limit of bolometric luminosity $\sim 10^{45.6}$ erg s^{-1}. However, we note that this bolometric correction may not be well quantified at $L_{2-10keV} < 10^{43.5}$ erg s^{-1}, since only a few sources in this range were included when deriving this bolometric correction. Thus, we are not able to make a conclusion based on X-ray data.

4.3.3. Test on Coadded Spectra

Here, we attempt another approach to probing the possibility of AGN activity in the sample, by utilizing the available rest-frame UV spectra of the ALPINE galaxies from DEIMOS and VIMOS. In a study of similar redshift galaxies drawn from the VUDS survey, Nakajima et al. (2018) proposed diagnostic diagrams for classifying the ionizing radiation field (star formation or AGN) of distant galaxies, using a combination of C III, C IV, and He II lines (also see Feltre et al. 2016; Le Fèvre et al. 2019). They tested a large grid of photoionization models and showed that these diagnostic diagrams could separate AGNs and SFGs, using a sample of C III-emitting galaxies at $z = 2 \sim 4$ detected in VUDS at high level of purity and completeness. Unfortunately, however, none of the spectra of the galaxies in the ALPINE sample cover the wavelength of the C III feature, and only the galaxies in our lower-redshift bin ($z \sim 4.5$) have spectra that cover the C IV and He II lines. Therefore, we combine the spectra of the C II-detected-lz subsample and measure the equivalent widths (EWs) of C IV and He II.

The spectra are combined (hereafter, "coadded") through an inverse variance–weighted average, after shifting each individual spectrum to the rest frame, interpolating onto a standard grid with a constant plate scale of $\lambda = \lambda_{\rm int}/(1 + z_{\rm min})$, where $\lambda_{\rm int}$ is the intrinsic plate scale specific to the instrument/setup and $z_{\rm min}$ is the minimum $z_{\rm spec}$ for each sample. Each spectrum is normalized to the average flux density in the rest-frame wavelength range $\lambda = 1350$–1400. The intrinsic plate scales were set to 0.47 Å for DEIMOS and 7.3 Å for VIMOS. Due to the differences of spectral resolution, the DEIMOS and VUDS spectra are coadded separately. Note that we use [C II] as the systemic redshift z_{spec} for each galaxy, as measurements with Lyα or ISM lines in the rest-frame UV do not necessarily probe the systemic redshift. For a total of 43 galaxies in the C II-detected-lz subsample, 42 galaxies

[25] CSTACK was developed by Takamitsu Miyaji and is available at http://lambic.astrosen.unam.mx/cstack/.

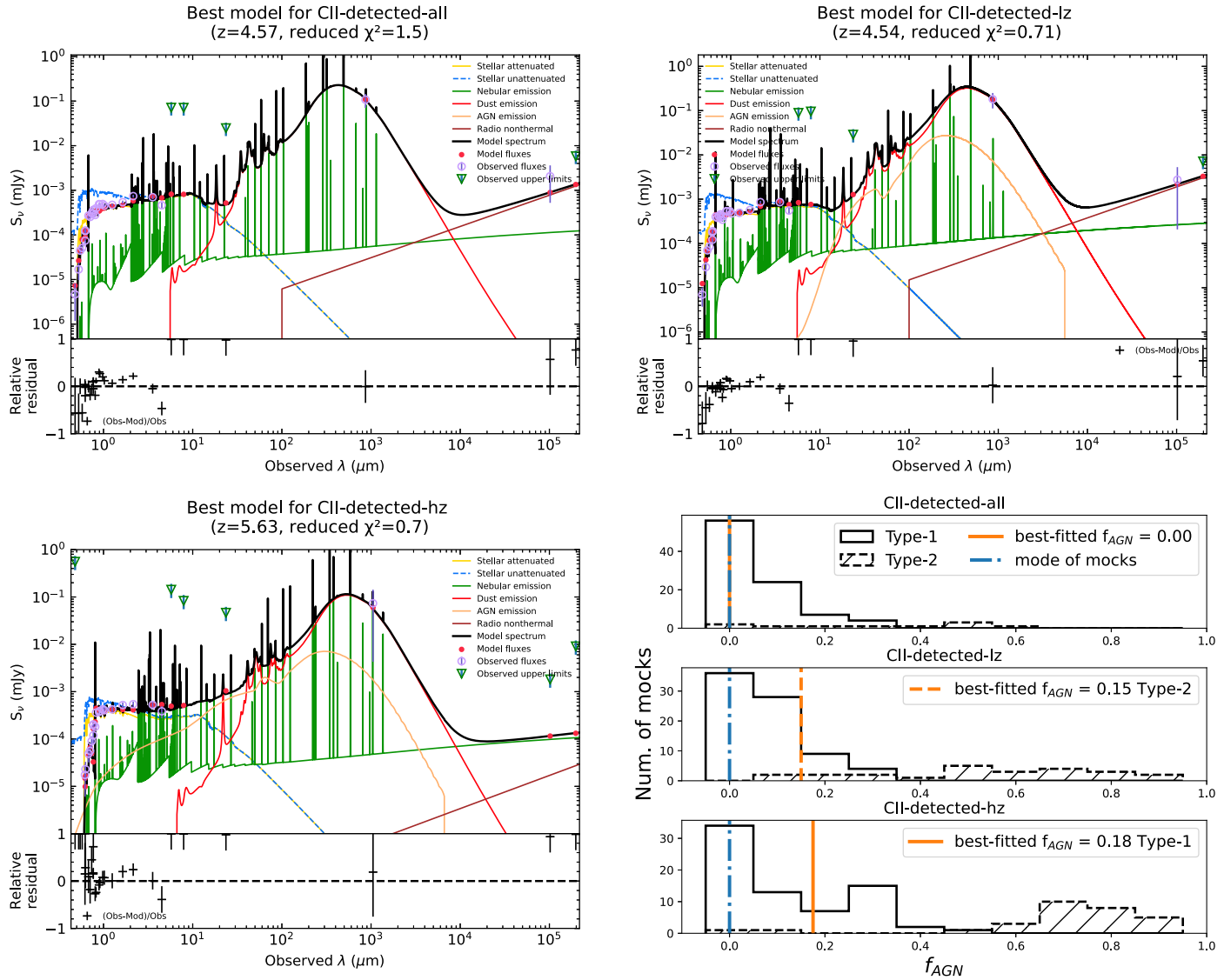

Figure 3. Top and bottom left: the best-fitting SED model from CIGALE for the C II-detected-all, C II-detected-lz, and C II-detected-hz stacks, from top to bottom, respectively. In each panel, the top shows the observed photometric fluxes with errors (purple), the 3σ upper limit fluxes (green triangles), the CIGALE-derived best model photometry (red dots), and the best-fitting CIGALE model (black). The best-fitting CIGALE model is the sum of the contributions from an AGN (orange), dust-attenuated stellar emission (yellow; the intrinsic stellar emission is indicated in blue), nebular emission (green), dust emission (red), and nonthermal radio emission (brown). The bottom shows the fractional discrepancies between the model and the photometry. The reduced χ^2 of the best-fitting models are indicated in the top labels. Bottom right: Histogram of the $f_{\rm AGN}$ of the C II-detected-all (top), C II-detected-lz (middle), and C II-detected-hz (bottom) subsamples, derived from 100 mocks, separated into type-1 (solid histograms) and type-2 (dashed histograms with hatching) AGNs, based on their fitted viewing angles. The best-fitting $f_{\rm AGN}$ are shown as the solid/dashed vertical orange lines for type-1/2 AGNs, respectively. The best-fitting AGN viewing angles are 70° and 30° for C II-detected-lz and C II-detected-hz, corresponding to type-2 and type-1 AGNs, respectively. The blue dashed lines mark the statistical mode of the mocks.

have spectra with rest-frame wavelength coverage of $\lambda = 1200$–1700, including 27 DEIMOS and 15 VIMOS spectra, while one galaxy has DEIMOS spectra up to rest-frame $\lambda = 1450$, which is excluded from this exercise. We measure the EWs of C IV and He II following the method described in Le Fèvre et al. (2019). Given the P Cygni profile of C IV, we use a double-Gaussian distribution to simultaneously fit the absorption and emission components. We measure the EW of He II using a single-Gaussian model. The coadded spectra of DEIMOS are shown in Figure 4, with zoom ins of C IV and He II shown to the right. The best-fitting line profiles are shown as red lines, with their EW values marked in the bottom of panels. No strong C IV and He II are observed. We derive EW(C IV) $= -2.23 \pm -0.38$, with the convention of negative EW indicating emission, and EW(C IV)/EW(He II) of 1.27 ± 0.27. These values and their uncertainties fall into the SFG region of the diagnostic diagrams (see Figure 11 in Nakajima et al. 2018). In addition, no other AGN features are shown in the coadded spectra, such as the N V 1240 emission. For the VUDS coadded spectra, C IV and He II are not detected, and thus we can draw no conclusions from these spectra, other than these features being very weak, which indicates little to no AGN activity.

To test whether one galaxy or a small set of galaxies might be dominating the results, despite the use of a normalization for all input spectra, we adopted a bootstrap analysis by randomly sampling the same number of galaxies as in our sample, with replacements, for the subset of galaxies with DEIMOS spectra, and measuring the EWs of C IV and He II. The bootstrap results are consistent with our measurements that these galaxies are not in the AGN region.

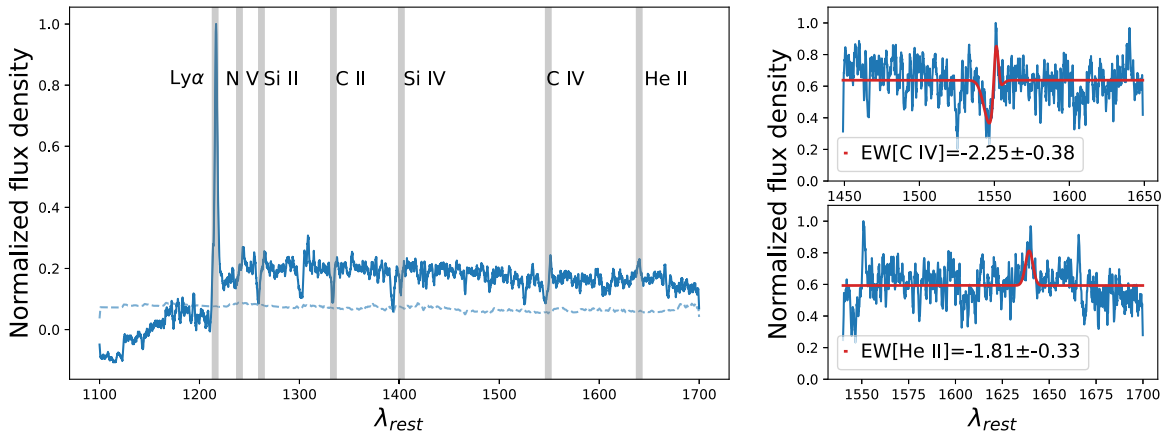

Figure 4. Left: inverse variance, unit-weighted coadded DEIMOS spectra of 27 ALPINE galaxies in the C II-detected-lz subsample. The variances of the coadded spectra are shown as the dashed lines. The important spectral features are indicated by the vertical dashed lines and are labeled. Right: zoom ins of the C IV and He II lines. The best-fitting line profiles are shown as red lines, with their EW values marked. The measured EW(C IV) vs. EW(C IV)/EW(He II) falls in the SFG region of the AGN/SFG diagnostic diagrams of Nakajima et al. (2018).

Overall, we do not find evidence of dominant AGN activity in any of our tests. Nevertheless, we note a caveat that we are not able to quantify the AGN contamination in the radio band, since AGNs could contribute in the radio band range over a factor of 10^5 among different AGN types (e.g., Panessa et al. 2019). However, the main contribution to the radio emission in radio-quiet AGNs, at least up to $z \sim 1.5$–2, is associated with star formation activity in the host, rather than with radio jets (Bonzini et al. 2015).

5. Discussion

We recover lower $q_{\rm TIR}$ values of our sample than the local $q_{\rm TIR}$ relation for normal SFGs at the $\sim 3\sigma$ significance level. However, our $q_{\rm TIR}$ values are consistent with a variety of $q_{\rm TIR}$ for high-redshift galaxies, including pure normal SFGs, SFGs plus AGNs, pure AGNs, and SMGs. In Section 4.3.1, we did not find evidence of dominant AGN activity with current multiwavelength photometry in any of our subsamples, and thus we dismiss the possibility of an AGN contribution as the dominant factor in lowering the $q_{\rm TIR}$. These results suggest that lower $q_{\rm TIR}$ values might be an intrinsic property of high-redshift ($z > 4$) SFGs. In this section, we discuss the possible genesis of recovering $q_{\rm TIR}$ values that are lower than measured in local counterparts, in terms of the effects of different assumptions on the radio spectral index (Section 5.1), the IR SED templates (Section 5.2), and astrophysical causes (Section 5.3).

5.1. The Effect of the Radio Spectral Index

The radio emission of SFGs consists of thermal and nonthermal emission (see Section 1 for further discussion). The thermal radio emission has a typical power-law spectrum with $\alpha = -0.1$, and the nonthermal emission has a much steeper spectrum with $\alpha = -0.8$. The relative contributions of the two emissions vary with frequency. The nonthermal emission dominates the lower frequency (<5 GHz) and thermal emission may dominate at frequencies >10 GHz (see also Price & Duric 1992). The fraction of thermal emission is found to be $f_{\rm th,1GHz} \sim 10\%$ at 1.4 GHz (Condon 1992; Niklas et al. 1997; Tabatabaei et al. 2017) and $f_{\rm th,10GHz} \sim 40\%$ at 10 GHz (Gioia et al. 1982; Klein et al. 1988, 2018). Our observation at 3 GHz corresponds to rest-frame 18 GHz at $z = 5$. Thus, the observed 3 GHz flux might be dominated by thermal emission, rather than nonthermal emission, at rest-frame 1.4 GHz. If we assume a fraction of thermal emission of 10% at 1 GHz and typical $\alpha = -0.1$ for thermal and $\alpha = -0.8$ for nonthermal spectra, the spectral index between the rest-frame 18 and 1.4 GHz is −0.60.

As mentioned in Section 4.1, the median α is found to be −0.8 for galaxies at $z > 2$ (Delhaize et al. 2017). Using $\alpha = -0.6$ and $\alpha = -0.8$, we recalculate $q_{\rm TIR}$s for the three subsamples, shown as the open and shaded blue markers in the right panels of Figure 2. Employing these spectral indices would slightly increase/decrease the $q_{\rm TIR}$ by 0.1 dex. Nevertheless, this relatively small change is not enough to explain our lower $q_{\rm TIR}$.

5.2. The Effect of the IR SED Templates

Since only a single monochromatic FIR data point is available from our observations, our estimated IR luminosity depends largely on the choice of IR SED template. Thus, we test whether a different IR SED template would change the IR luminosity enough to dramatically alter the recovered $q_{\rm TIR}$. As mentioned in Béthermin et al. (2020), several works have constructed IR SED empirical templates up to $z \sim 4$ (Béthermin et al. 2015, Álvarez-Márquez et al. 2016; 2017; Schreiber et al. 2018; Álvarez-Márquez et al. 2019). Here, we consider several other SED templates that might be representative of the average IR SED of our ALPINE galaxies, and calculate the difference between the fiducial $L_{\rm IR}$ and the $L_{\rm IR}$ using our primary IR SED template. As a reminder, the primary IR SED template is adopted from Béthermin et al. (2015), with $\langle U \rangle = 50$ corresponding to the dust temperature $T_d \sim 41$K (see Sections 3.2 and 4.2). This is consistent with the T_d measured for four normal SFGs at $z = 5.5$ using observations in three ALMA bands (Faisst et al. 2020a). The changes in $q_{\rm TIR}$ when using the different templates are summarized in Table 4.

First, we consider other possible SED templates from Béthermin et al. (2015). In detail, Béthermin et al. (2015) measured the evolution of the average SED by varying the $\langle U \rangle$ parameter and using a sample of massive ($>3 \times 10^{10}$) main-sequence SFGs and starbursts in the COSMOS field. They found that the stacked SED for main-sequence SFGs in the redshift range of $3.5 < z < 4.0$ was best fitted to the SED template with $\langle U \rangle = 72.98$. Such a template yields a slightly larger fiducial $L_{\rm IR}$, increasing the primary $L_{\rm IR}$ by 0.07 dex.

Second, we consider six possible SED templates constructed by Schreiber et al. (2018). They presented an SED library

Table 4
Possible IR SED Templates and the Change in the Recovered $q_{\rm TIR}$

Template (1)	Criteria (2)	$\Delta\ q_{\rm TIR}$ [dex] (3)
Béthermin et al. (2015)	$\langle U\rangle = 50$	
Béthermin et al. (2015)	$\langle U\rangle = 72.98$	+0.07
Schreiber et al. (2018)	$T_d = 41.8$ K, 44.4 K, 49.0 K, and a fixed IR8 = 7.37	+0.12, +0.19, and +0.34
Schreiber et al. (2018)	$T_d = 41.8$ K, 44.4 K, 49.0 K, and a fixed IR8 = 10.7	+0.07, +0.15, and +0.30
De Rossi et al. (2018)	Haro 11	−0.4
Álvarez-Márquez et al. (2019)	$U_{\rm min} = 30.9$ and 36.9	−0.59 and −0.52

characterized by the dust mass and the mid-to-total IR color (IR8). Applying this library to SFGs at $0.5 < z < 4$ in the deep CANDELS fields, using both individual detections and stacks of Herschel and ALMA imaging, they found trends of increasing T_d and IR8 with redshift and distance from the main sequence. We include the best-fitting SED template of the SFGs in their highest-redshift bin ($3.5 < z < 5.0$), which is characterized by T_d of 41.8 K and IR8 of 7.37. Following the T_d and IR8 relation (Equations (15) and (16) in Schreiber et al. 2018), the T_d are found to be 44.4 K and 49.0 K at z = 4.5 and z = 5.5, with a fixed IR8 = 7.37. In addition, Schreiber et al. (2018) found in general higher IR8 values for low-mass galaxies ($M_* < 10^{10} M_\odot$) up to $z \sim 2$, which is comparable with the median stellar mass of the C II-detected-all subsample ($10^{9.78}\ M_\odot$). Thus, we also include templates with a higher IR8 (IR8 = 10.7) that are best fitted to low-mass galaxies at $1.2 < z < 1.8$. Using the combination of three T_d and two IR8 values, we recalculate the $q_{\rm TIR}$ and obtain an average increase of 0.2 dex in IR luminosity (see the changes using each template in Table 4). Thus, we add an additional 0.2 dex in our $L_{\rm IR}$ values and plot the corresponding fiducial $q_{\rm TIR}$ as the open orange markers in the right panel of Figure 2.

Third, we consider the SED library constructed by Álvarez-Márquez et al. (2019), using the CIGALE SED fitting code and fitted to a large sample of Lyman-break galaxies at redshift $2.5 < z < 3.5$ in the COSMOS field, binned in terms of stellar mass, UV luminosity ($L_{\rm FUV}$), and UV continuum slope (β). We use the best-fitting SED template for their lower-mass galaxies (LBG-M1: $\log(M_*/M_\odot) = 9.75$–10.00 and LBG-M2: $\log(M_*/M_\odot)$ 10.00–10.25). We calculate a smaller fiducial $L_{\rm IR}$, decreasing the primary $L_{\rm IR}$ by 0.59 dex and 0.52 dex. This might be due to these templates having lower $U_{\rm min}$ ($U_{\rm min}$ = 30.9 and 36.9 for the two lower-mass bins), which corresponds to a lower T_d as compared to the templates in Schreiber et al. (2018) and Béthermin et al. (2015). To show the change in $q_{\rm TIR}$ when using these IR SED templates, we reduce our $L_{\rm IR}$ values by 0.5 dex and plot the corresponding fiducial $q_{\rm TIR}$ as the shaded orange markers in the right panel of Figure 2.

Finally, we consider the SED template constructed by De Rossi et al. (2018), based on the SED of Haro 11, a local moderately low-metallicity galaxy undergoing a very young and vigorous starburst that could be similar to the conditions of high-redshift galaxies. They showed a high level of consistency with the Haro 11 SED template and the measurements of individual galaxies at $z > 5$, with adequate FIR observations. We obtain a smaller fiducial $L_{\rm IR}$ by decreasing the primary $L_{\rm IR}$ by 0.4 dex.

We find that the estimated $L_{\rm IR}$ depends on the adopted IR SED template and the assumption of dust temperature. Applying different IR templates can change the $q_{\rm TIR}$ more significantly and place a tension between our stacked $q_{\rm TIR}$s and those of local SFGs at the $<1\sigma$ significance level.

5.3. Astrophysical Causes

As mentioned previously, the radio emission in the SFGs directly originates from the star formation process, and is expected to reflect the SFR on a relatively short timescale. However, the IR emission is due to the energy from star formation that is absorbed and reemitted by dust, which depends on the amount of dust, quantified as the dust attenuation. Thus, if the IR and radio emission originate purely from star formation, the IRRC should be proportional to the dust attenuation. If the dust attenuation of ALPINE galaxies is lower than that of local SFGs, it would depress the IR emission and result in a lower $q_{\rm TIR}$ when compared to that of local SFGs.

Indeed, Fudamoto et al. (2020) have studied the dust attenuation of ALPINE galaxies, in terms of the UV spectral slope (β), M_*, and IR excess ($\rm IRX = L_{IR}/L_{UV}$). They found lower IRX values for individual ALPINE galaxies and also for stacks, implying a lower obscured fraction of star formation than at lower redshift. Fudamoto et al. (2020) measured the obscured fraction of star formation ($f_{\rm obs} = \rm SFR_{IR}/SFR_{total}$) by stacking ALPINE galaxies in different stellar mass and redshift bins. For $M_* > 10^{10} M_\odot$, the stacked $f_{\rm obs}$ is $0.67^{+0.05}_{-0.07}$ at $z \sim 4.5$ and 0.44 ± 0.11 at $z \sim 5.5$, as compared to $f_{obs} > 0.80$ at $z = 0$–2.5 at the same stellar mass. At lower mass, $M_* < 10^{10} M_\odot$, the $f_{\rm obs}$ is much lower, with $0.36^{+0.13}_{-0.19}$ at $z \sim 4.5$ and a 3σ upper limit of $f_{\rm obs} < 0.43$ at $z \sim 5.5$, similar to $f_{\rm obs}$ at $z = 2.5$, but lower than ∼0.6 at $z = 0$. It is possible that the dust buildup, which primarily governs the IR emission, in addition to older stellar populations, does not have enough time to occur fully in these galaxies, whereas the radio emission can occur on a more rapid timescale. For simplicity, we assume $f_{\rm obs} = 0.5$ for our ALPINE galaxies and $f_{\rm obs} = 0.8$ at $z = 0$. We find that, under these assumptions, the $q_{\rm TIR}$ values increase by 0.2 dex, as shown by the open green markers in the right panel of Figure 2, which places a tension between our stacked $q_{\rm TIR}$s and those of local SFGs at the $<1\sigma$ significance level.

Nevertheless, slightly brighter normal SFGs at high redshift might have similar obscured fractions as local SFGs. Bowler et al. (2022) measured the dust continuum of five normal SFGs at $z \sim 7$, and found that the IRX–β relations in these galaxies were consistent with the IRX–β relations of local starburst galaxies. However, these galaxies are three times brighter in rest-frame UV than our ALPINE galaxies, on average. Thus, their obscured fraction might be different from our sample.

There are some other possible explanations for the lower $q_{\rm TIR}$. Recently, Algera et al. (2020) have shown that either increasing the magnetic field or decreasing the density of the ISM by a factor of 5 could decrease the $q_{\rm TIR}$ by 0.2 dex up to $z \sim 4$. In addition, Bressan et al. (2002) found that the $q_{\rm TIR}$ is dependent on the stage of evolution of the stellar populations in the galaxy. They suggested that, in the poststarburst phase, nonthermal synchrotron emission dominates, thus increasing the apparent radio flux. By

modeling different star formation histories with e-folding timescales in the range of 10–50 Myr, they found that, in all models, the $q_{\rm TIR}$s decrease with time and reach $q_{\rm TIR} < 2$ after ∼25 Myr, then remain at $q_{\rm TIR} < 2$ for another ∼20 Myr. Although, we are not able to quantitatively test these hypotheses with our data, due to a lack of information, such as ISM density, magnetic field, and stellar age, it is plausible that the ISM densities are higher in ALPINE galaxies, since galaxies are found to be more compact at high z (van Dokkum et al. 2010; van der Wel et al. 2014) and contain a larger ISM gas content at high z (Santini et al. 2014).

6. Summary

We have studied the radio properties of 66 galaxies in the COSMOS field that have [C II] detections from the ALPINE survey, by exploiting the stacking technique. We separated them into three subsamples, depending on their spectroscopic redshift, named C II-detected-all, lz, and hz. We detected radio signals for C II-detected-all and lz in their median-stacked 3 GHz images, and placed meaningful limits on the C II-detected-hz subsample. Our main conclusions are as follows.

1. We recovered lower $q_{\rm TIR}$ values of our stacked samples at $z \sim 4.6$ than the local $q_{\rm TIR}$ relation for normal SFGs at the $\sim 3\sigma$ significance level. However, our $q_{\rm TIR}$ values are broadly consistent with those of SMGs at $2 < z < 5$ and all galaxies, including SFGs plus AGNs and pure AGNs, at $z \sim 3$.
2. While powerful broad-line AGNs were selected against when constructing the ALPINE sample, the prevalence of lower-luminosity and/or obscured AGNs was previously unknown. Although the data are not sufficient to confirm whether AGNs contribute to the radio band, either through spectral index or SFR estimates, our samples do not exhibit evidence of dominant AGN activity in the stacked optical-to-FIR SED, X-ray, and UV spectra, which rules out the possibility of the AGN component being the main contributor to the observed deviation. The stacked SEDs of all three subsamples best fit little to no AGN activity, and their $f_{\rm AGN}$ mocks dominate the lower-$f_{\rm AGN}$ ($f_{\rm AGN} \leqslant 0.2$) regions. The coadded UV spectra of C II-detected-lz show no evidence of AGN activity. The upper limits of $L_{\rm AGN}$ from stacked SEDs and X-ray are $<10^{45.6}$ erg s^{-1}.
3. We explore various effects that might reduce the tension between our stacked $q_{\rm TIR}$ values and those of local SFGs, including changing the fiducial radio spectral index and applying different IR templates. Either of these can reduce the tension to the $<1\sigma$ level.
4. In addition, such a tension can be alleviated, based on the fact that a lower obscured fraction of star formation has been found in ALPINE galaxies than in local galaxies and even in galaxies at $z \sim 2$ (Fudamoto et al. 2020). It is possible that the dust buildup, which primarily governs the IR emission, in addition to older stellar populations, has not had enough time to occur fully in these galaxies, whereas the radio emission can respond on a more rapid timescale. Thus, we might expect the IRRC to be modified at high redshift.

Future observations of a large sample of normal high-redshift SFGs will be essential for testing whether the lower $q_{\rm TIR}$ are ubiquitous in these galaxies. Indeed, we expect that future JWST projects with observations at MIR, such as CEERS and PRIMER, could provide stronger constraints on the dust-obscured star formation and AGN activities of high-redshift galaxies. In addition, we expect that combined deeper radio and FIR observations in more than one band will provide a robust way of calculating the $q_{\rm TIR}$ and studying the evolution of the IRRC.

L.S. acknowledges the National Natural Science Foundation of China (NSFC) grant No. 12003030 and Fundamental Research Funds for the Central Universities. G.L. acknowledges research grants from the China Manned Space Project (No. CMS-CSST-2021-A06 and No. CMS-CSST-2021-A07), as well as the NSFC grant No. 11421303. W.F. acknowledges the NSFC grant No. 11773024. This work is also based in part on observations taken by the 3D-HST Treasury Program (GO 12177 and 12328) with the NASA/ESA HST, which is operated by the Association of Universities for Research in Astronomy, Inc., under NASA contract NAS5-26555. Part of the material presented herein is based upon work supported by the National Aeronautics and Space Administration under NASA grant no. 80NSSC21K0986. This material is based upon work supported by the National Science Foundation under grant No. 1908422. M.B. gratefully acknowledges support from the ANID BASAL project FB210003 and the FONDECYT regular grant 1211000. G.C.J. acknowledges ERC Advanced Grants 695671 "QUENCH" and 789056 "First Galaxies," as well as support from the Science and Technology Facilities Council (STFC). M.R. acknowledges support from Narodowe Centrum Nauki (UMO-2020/38/E/ST9/00077). E.S. thanks the LSSTC Data Science Fellowship Program, which is funded by LSSTC, NSF Cybertraining Grant #1829740, the Brinson Foundation, and the Moore Foundation. E.I. acknowledges funding from ANID FONDECYT Regular 1221846.

This paper is based on data obtained with the ALMA Observatory, under Large Program 2017.1.00428.L. ALMA is a partnership of ESO (representing its member states), NSF (USA), and NINS (Japan), together with NRC (Canada), MOST, and ASIAA (Taiwan), and KASI (Republic of Korea), in cooperation with the Republic of Chile. The Joint ALMA Observatory is operated by ESO, AUI/NRAO, and NAOJ. This study is based on data taken with the Karl G. Jansky Very Large Array, which is operated by the National Radio Astronomy Observatory. The National Radio Astronomy Observatory is a facility of the National Science Foundation operated under cooperative agreement by Associated Universities, Inc. This work is based in part on observations made with the Spitzer Space Telescope, which is operated by the Jet Propulsion Laboratory, California Institute of Technology, under a contract with NASA. Furthermore, this work is based on data from the W.M. Keck Observatory, the Canada–France–Hawaii Telescope, the Subaru Telescope, and data retrieved from the HSC data archive system, which is operated by the Subaru Telescope and Astronomy Data Center at the National Astronomical Observatory of Japan. We wish to thank the indigenous Hawaiian community for allowing us to be guests on their sacred mountain, a privilege, without which this work would not have been possible. We are most fortunate to have been able to conduct observations from this site.

Appendix A
Optical/IR/Radio Stacks

To illustrate the data quality of the stacks, in Figure 5 we show the stack cutouts of all the available bands for the C II-detected-all sample.

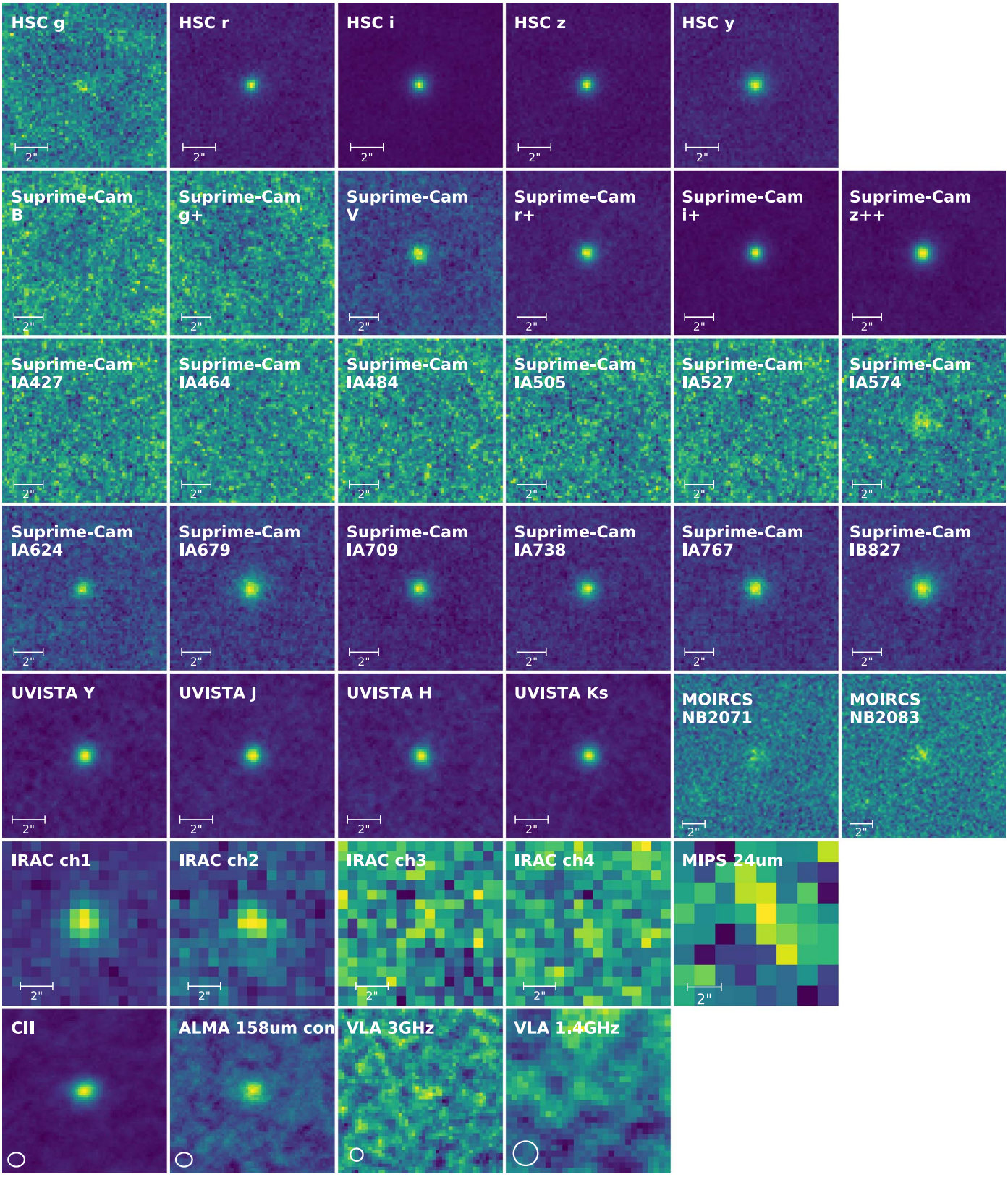

Figure 5. The $10'' \times 10''$ stack cutouts of all the available bands for the C II-detected-all sample. The wavelength generally increases from top left to bottom right. The instrument and band are listed for each cutout. See Section 3.1 for the stacking method.

Appendix B
Test on CIGALE SED Fitting with Current Photometry Set

We use the CIGALE SED fitting to rule out the possibility of considerable obscured and unobscured AGN activity among the ALPINE sample. We apply a mock analysis in CIGALE in order to check the reliability of the estimated parameters. However, due to the upper limits given at 5.8 μm, 8 μm, and 24 μm, the SED constraint on AGN activity is limited, especially for type-2 AGNs, which is also indicated by the large uncertainties on $f_{\rm AGN}$.

To further test the efficacy of the CIGALE SED fitting in constraining AGN activity with the current photometry set, a grid of synthetic models is created by CIGALE using the best-fitting parameters for the stacked SED of the C II-detected-all sample. For this test, the $f_{\rm AGN}$ is allowed to vary between 0–0.9, and the viewing angle is set to $\theta = 30°$ for type-1 and $\theta = 70°$ for type-2 AGNs. For each synthetic model, we generate 100 mock sources, by assigning mock fluxes based on the fluxes from the model and using an S/N equivalent to that of the corresponding stacked photometry. In detail, the mock flux densities in a given band are assigned by initially randomly sampling a Gaussian distribution with a mean equal to the model flux and an error appropriate for the S/N of a given data point in the stacked photometry, effectively reproducing a photometric measurement of the model spectrum. For those bands where only upper limits are available (e.g., IRAC channels 3, 4, and MIPS 24 μm), we set the mock flux densities in these bands by multiplying the model flux density by 40–90, in order to match the ratio of the 3σ upper limits and best-fitting model values (∼86, 87, and 47 for IRAC channels 3, 4, and MIPS 24 μm, respectively). The $f_{\rm AGN}$ of type-1 AGNs are well recovered in the full $f_{\rm AGN}$ range, with small uncertainty (∼0.1), while those of type-2 AGNs have larger uncertainties and are slightly offset to lower $f_{\rm AGN}$ values for $f_{\rm AGN} <= 0.5$. These results suggest that, with the current photometry set, CIGALE can robustly recover $f_{\rm AGN}$ for type-1 AGNs in the full $f_{\rm AGN}$ range and type-2 AGNs in the high-$f_{\rm AGN}$ range, while for type-2 sources with low-to-moderate $f_{\rm AGN}$, $f_{\rm AGN}$ could be underestimated by a factor of 2.

ORCID iDs

Lu Shen https://orcid.org/0000-0001-9495-7759
Brian C. Lemaux https://orcid.org/0000-0002-1428-7036
Lori M. Lubin https://orcid.org/0000-0003-2119-8151
Guilin Liu https://orcid.org/0000-0003-2390-7927
Matthieu Béthermin https://orcid.org/0000-0002-3915-2015
Médéric Boquien https://orcid.org/0000-0003-0946-6176
Olga Cucciati https://orcid.org/0000-0002-9336-7551
Margherita Talia https://orcid.org/0000-0003-4352-2063
Daniela Vergani https://orcid.org/0000-0003-0898-2216
Gianni Zamorani https://orcid.org/0000-0002-2318-301X
Andreas L. Faisst https://orcid.org/0000-0002-9382-9832
Michele Ginolfi https://orcid.org/0000-0002-9122-1700
Carlotta Gruppioni https://orcid.org/0000-0002-5836-4056
Sandro Bardelli https://orcid.org/0000-0002-8900-0298
Nimish Hathi https://orcid.org/0000-0001-6145-5090
Anton M. Koekemoer https://orcid.org/0000-0002-6610-2048
Michael Romano https://orcid.org/0000-0002-9948-3916
Daniel Schaerer https://orcid.org/0000-0001-7144-7182
Elena Zucca https://orcid.org/0000-0002-5845-8132
Wenjuan Fang https://orcid.org/0000-0003-4987-7340
Ben Forrest https://orcid.org/0000-0001-6003-0541
Roy Gal https://orcid.org/0000-0001-8255-6560
Denise Hung https://orcid.org/0000-0001-7523-140X
Ekta A. Shah https://orcid.org/0000-0001-7811-9042
Priti Staab https://orcid.org/0000-0002-8877-4320
Brittany Vanderhoof https://orcid.org/0000-0002-8163-0172

References

Algera, H. S. B., Smail, I., Dudzevičiūtė, U., et al. 2020, ApJ, 903, 138
Álvarez-Márquez, J., Burgarella, D., Buat, V., Ilbert, O., & Pérez-González, P. G. 2019, A&A, 630, A153
Álvarez-Márquez, J., Burgarella, D., Heinis, S., et al. 2016, A&A, 587, A122
An, F., Vaccari, M., Smail, I., et al. 2021, MNRAS, 507, 2643
Appleton, P. N., Fadda, D. T., Marleau, F. R., et al. 2004, ApJS, 154, 147
Arnouts, S., Cristiani, S., Moscardini, L., et al. 1999, MNRAS, 310, 540
Astropy Collaboration, Robitaille, T. P., Tollerud, E. J., et al. 2013, A&A, 558, A33
Astropy Collaboration, Price-Whelan, A. M., Sipőcz, A. M., et al. 2018, AJ, 156, 123
Becker, R. H., White, R. L., & Helfand, D. J. 1995, ApJ, 450, 559
Bell, E. F., McIntosh, D. H., Katz, N., & Weinberg, M. D. 2003, ApJS, 149, 289
Bertin, E., & Arnouts, S. 1996, A&AS, 117, 393
Bertoldi, F., Carilli, C., Aravena, M., et al. 2007, ApJS, 172, 132
Béthermin, M., Daddi, E., Magdis, G., et al. 2015, A&A, 573, A113
Béthermin, M., Fudamoto, Y., Ginolfi, M., et al. 2020, A&A, 643, A2
Béthermin, M., Wu, H.-Y., Lagache, G., et al. 2017, A&A, 607, A89
Bonzini, M., Mainieri, V., Padovani, P., et al. 2015, MNRAS, 453, 1079
Boquien, M., Burgarella, D., Roehlly, Y., et al. 2019, A&A, 622, A103
Bourne, N., Dunne, L., Ivison, R. J., et al. 2011, MNRAS, 410, 1155
Bowler, R. A. A., Cullen, F., McLure, R. J., Dunlop, J. S., & Avison, A. 2022, MNRAS, 510, 5088
Bressan, A., Silva, L., & Granato, G. L. 2002, A&A, 392, 377
Brisbin, D., Miettinen, O., Aravena, M., et al. 2017, A&A, 608, A15
Bruzual, G., & Charlot, S. 2003, MNRAS, 344, 1000
Calistro Rivera, G., Williams, W. L., Hardcastle, M. J., et al. 2017, MNRAS, 469, 3468
Calzetti, D., Armus, L., Bohlin, R. C., et al. 2000, ApJ, 533, 682
Capak, P., Cowie, L. L., Hu, E. M., et al. 2004, AJ, 127, 180
Carilli, C. L., Lee, N., Capak, P., et al. 2008, ApJ, 689, 883
Casey, C. M., Berta, S., Béthermin, M., et al. 2012, ApJ, 761, 140
Chabrier, G. 2003, PASP, 115, 763
Ciesla, L., Charmandaris, V., Georgakakis, A., et al. 2015, A&A, 576, A10
Civano, F., Marchesi, S., Comastri, A., et al. 2016, ApJ, 819, 62
Condon, J. J. 1992, ARA&A, 30, 575
de Jong, T., Klein, U., Wielebinski, R., & Wunderlich, E. 1985, A&A, 147, L6
De Rossi, M. E., Rieke, G. H., Shivaei, I., Bromm, V., & Lyu, J. 2018, ApJ, 869, 4
Del Moro, A., Alexander, D. M., Mullaney, J. R., et al. 2013, A&A, 549, A59
Delhaize, J., Smolčić, V., Delvecchio, I., et al. 2017, A&A, 602, A4
Delvecchio, I., Daddi, E., Sargent, M. T., et al. 2021, A&A, 647, A123
Donley, J. L., Rieke, G. H., Rigby, J. R., & Pérez-González, P. G. 2005, ApJ, 634, 169
Draine, B. T., Aniano, G., Krause, O., et al. 2014, ApJ, 780, 172
Faisst, A. L., Fudamoto, Y., Oesch, P. A., et al. 2020a, MNRAS, 498, 4192
Faisst, A. L., Schaerer, D., Lemaux, B. C., et al. 2020b, ApJS, 247, 61
Feltre, A., Charlot, S., & Gutkin, J. 2016, MNRAS, 456, 3354
Fudamoto, Y., Oesch, P. A., Faisst, A., et al. 2020, A&A, 643, A4
Garn, T., Green, D. A., Riley, J. M., & Alexander, P. 2009, MNRAS, 397, 1101
Garrett, M. A. 2002, A&A, 384, L19
Giacconi, R., Zirm, A., Wang, J., et al. 2002, ApJS, 139, 369
Gioia, I. M., Gregorini, L., & Klein, U. 1982, A&A, 116, 164
Gürkan, G., Hardcastle, M. J., Smith, D. J. B., et al. 2018, MNRAS, 475, 3010
Hasinger, G., Capak, P., Salvato, M., et al. 2018, ApJ, 858, 77
Helou, G., & Bicay, M. D. 1993, ApJ, 415, 93
Helou, G., Soifer, B. T., & Rowan-Robinson, M. 1985, ApJL, 298, L7
Ibar, E., Ivison, R. J., Best, P. N., et al. 2010, MNRAS, 401, L53
Ibar, E., Ivison, R. J., Biggs, A. D., et al. 2009, MNRAS, 397, 281
Ibar, E., Cirasuolo, M., Ivison, R., et al. 2008, MNRAS, 386, 953
Ichikawa, T., Suzuki, R., Tokoku, C., et al. 2006, Proc. SPIE, 6269, 626916

Ilbert, O., Arnouts, S., McCracken, H. J., et al. 2006, A&A, 457, 841
Ilbert, O., Salvato, M., Capak, P., et al. 2008, in ASP Conf. Ser. 399, Panoramic Views of Galaxy Formation and Evolution, ed. T. Kodama, T. Yamada, & K. Aoki (San Francisco, CA: ASP), 169
Ivison, R. J., Magnelli, B., Ibar, E., et al. 2010, A&A, 518, L31
Jarvis, M. J., Smith, D. J. B., Bonfield, D. G., et al. 2010, MNRAS, 409, 92
Jiménez-Andrade, E. F., Magnelli, B., Karim, A., et al. 2019, A&A, 625, A114
Karim, A., Schinnerer, E., Martínez-Sansigre, A., et al. 2011, ApJ, 730, 61
Khusanova, Y., Le Fèvre, O., Cassata, P., et al. 2020, A&A, 634, A97
Klein, U., Lisenfeld, U., & Verley, S. 2018, A&A, 611, A55
Klein, U., Wielebinski, R., & Morsi, H. W. 1988, A&A, 190, 41
Koekemoer, A. M., Aussel, H., Calzetti, D., et al. 2007, ApJS, 172, 196
Lacki, B. C., & Thompson, T. A. 2010, ApJ, 717, 196
Laigle, C., McCracken, H. J., Ilbert, O., et al. 2016, ApJS, 224, 24
Le Fèvre, O., Béthermin, M., Faisst, A., et al. 2020, A&A, 643, A1
Le Fèvre, O., Lemaux, B. C., Nakajima, K., et al. 2019, A&A, 625, A51
Le Fèvre, O., Tasca, L. A. M., Cassata, P., et al. 2015, A&A, 576, A79
Le Fèvre, O., Vettolani, G., Garilli, B., et al. 2005, A&A, 439, 845
Le Floc'h, E., Aussel, H., Ilbert, O., et al. 2009, ApJ, 703, 222
Lemaux, B. C., Cucciati, O., Le Fèvre, O., et al. 2022, A&A, 662, A33
Lemaux, B. C., Le Fèvre, O., Cucciati, O., et al. 2018, A&A, 615, A77
Lemaux, B. C., Le Floc'h, E., Le Fèvre, O., et al. 2014, A&A, 572, A90
Leslie, S. K., Schinnerer, E., Liu, D., et al. 2020, ApJ, 899, 58
Lubin, L. M., Gal, R. R., Lemaux, B. C., Kocevski, D. D., & Squires, G. K. 2009, AJ, 137, 4867
Lutz, D., Poglitsch, A., Altieri, B., et al. 2011, A&A, 532, A90
Lyu, J., & Rieke, G. H. 2017, ApJ, 841, 76
Lyu, J., Rieke, G. H., & Shi, Y. 2017, ApJ, 835, 257
Magdis, G. E., Daddi, E., Béthermin, M., et al. 2012, ApJ, 760, 6
Magnelli, B., Ivison, R. J., Lutz, D., et al. 2015, A&A, 573, A45
Mallery, R. P., Mobasher, B., Capak, P., et al. 2012, ApJ, 760, 128
Man, A. W. S., Greve, T. R., Toft, S., et al. 2016, ApJ, 820, 11
Mao, M. Y., Huynh, M. T., Norris, R. P., et al. 2011, ApJ, 731, 79
Marchesi, S., Civano, F., Elvis, M., et al. 2016a, ApJ, 817, 34
Marchesi, S., Civano, F., Salvato, M., et al. 2016b, ApJ, 827, 150
Marchesi, S., Lanzuisi, G., Civano, F., et al. 2016c, ApJ, 830, 100
Michałowski, M. J., Watson, D., & Hjorth, J. 2010, ApJ, 712, 942
Miettinen, O., Delvecchio, I., Smolčić, V., et al. 2017, A&A, 597, A5
Miller, N. A., Bonzini, M., Fomalont, E. B., et al. 2013, ApJS, 205, 13
Miyaji, T., & Griffiths, R. E. 2008, AAS/HEAD Meeting, 10, 4.01
Molnár, D. C., Sargent, M. T., Leslie, S., et al. 2021, MNRAS, 504, 118
Mor, R., & Netzer, H. 2012, MNRAS, 420, 526
Mullaney, J. R., Pannella, M., Daddi, E., et al. 2012, MNRAS, 419, 95
Murphy, E. J. 2009, ApJ, 706, 482
Nakajima, K., Schaerer, D., Le Fèvre, O., et al. 2018, A&A, 612, A94
Niklas, S., Klein, U., & Wielebinski, R. 1997, A&A, 322, 19
Oliver, S. J., Bock, J., Altieri, B., et al. 2012, MNRAS, 424, 1614
Padovani, P., Alexander, D. M., Assef, R. J., et al. 2017, A&ARv, 25, 2
Panessa, F., Baldi, R. D., Laor, A., et al. 2019, NatAs, 3, 387
Pearson, W. J., Wang, L., Hurley, P. D., et al. 2018, A&A, 615, A146
Price, R., & Duric, N. 1992, ApJ, 401, 81
Ramos Padilla, A. F., Wang, L., Małek, K., Efstathiou, A., & Yang, G. 2022, MNRAS, 510, 687
Romano, M., Cassata, P., Morselli, L., et al. 2021, A&A, 653, A111
Runnoe, J. C., Brotherton, M. S., & Shang, Z. 2012, MNRAS, 422, 478
Sajina, A., Yan, L., Lutz, D., et al. 2008, ApJ, 683, 659
Sanders, D. B., Salvato, M., Aussel, H., et al. 2007, ApJS, 172, 86
Santini, P., Maiolino, R., Magnelli, B., et al. 2014, A&A, 562, A30
Sargent, M. T., Schinnerer, E., Murphy, E., et al. 2010, ApJL, 714, L190
Schinnerer, E., Carilli, C. L., Capak, P., et al. 2008, ApJL, 689, L5
Schinnerer, E., Sargent, M. T., Bondi, M., et al. 2010, ApJS, 188, 384
Schinnerer, E., Smolčić, V., Carilli, C. L., et al. 2007, ApJS, 172, 46
Schleicher, D. R. G., & Beck, R. 2013, A&A, 556, A142
Schreiber, C., Elbaz, D., Pannella, M., et al. 2018, A&A, 609, A30
Scoville, N., Abraham, R. G., Aussel, H., et al. 2007, ApJS, 172, 38
Shen, L., Lemaux, B. C., Lubin, L. M., et al. 2020, MNRAS, 494, 5374
Shen, L., Lemaux, B. C., Lubin, L. M., et al. 2021, ApJ, 912, 60
Shen, L., Miller, N. A., Lemaux, B. C., et al. 2017, MNRAS, 472, 998
Smith, D. J. B., Jarvis, M. J., Hardcastle, M. J., et al. 2014, MNRAS, 445, 2232
Smith, D. J. B., Haskell, P., Gürkan, G., et al. 2021, A&A, 648, A6
Smolčić, V., Delvecchio, I., Zamorani, G., et al. 2017b, A&A, 602, A2
Smolčić, V., Karim, A., Miettinen, O., et al. 2015, A&A, 576, A127
Smolčić, V., Novak, M., Bondi, M., et al. 2017a, A&A, 602, A1
Smolčić, V., Novak, M., Delvecchio, I., et al. 2017c, A&A, 602, A6
Speagle, J. S., Steinhardt, C. L., Capak, P. L., & Silverman, J. D. 2014, ApJS, 214, 15
Steinhardt, C. L., Speagle, J. S., Capak, P., et al. 2014, ApJL, 791, L25
Sutherland, W., & Saunders, W. 1992, MNRAS, 259, 413
Suzuki, R., Tokoku, C., Ichikawa, T., et al. 2008, PASJ, 60, 1347
Symeonidis, M., Giblin, B. M., Page, M. J., et al. 2016, MNRAS, 459, 257
Tabatabaei, F. S., Schinnerer, E., Krause, M., et al. 2017, ApJ, 836, 185
Tasca, L. A. M., Le Fèvre, O., Hathi, N. P., et al. 2015, A&A, 581, A54
Tasca, L. A. M., Le Fèvre, O., Ribeiro, B., et al. 2017, A&A, 600, A110
Thomson, A. P., Ivison, R. J., Simpson, J. M., et al. 2014, MNRAS, 442, 577
Tomczak, A. R., Quadri, R. F., Tran, K.-V. H., et al. 2016, ApJ, 817, 118
van der Wel, A., Franx, M., van Dokkum, P. G., et al. 2014, ApJ, 788, 28
van Dokkum, P. G., Whitaker, K. E., Brammer, G., et al. 2010, ApJ, 709, 1018
Voelk, H. J. 1989, A&A, 218, 67
Yang, G., Boquien, M., Buat, V., et al. 2020, MNRAS, 491, 740
Yun, M. S., Reddy, N. A., & Condon, J. J. 2001, ApJ, 554, 803